Retina-Inspired Artificial Synapses and Near-Infrared Optoelectronic Neurostimulation Devices Using Quantum Dots

by

Rıdvan Balamur

A Dissertation Submitted to the
Graduate School of Sciences and Engineering
in Partial Fulfillment of the Requirements for
the Degree of

Master of Science

in

Electrical and Electronics Engineering

KOÇ ÜNİVERSİTESİ

August 12, 2024

Retina-Inspired Artificial Synapses and Near-Infrared Optoelectronic Neurostimulation Devices Using Quantum Dots

Koç University

Graduate School of Sciences and Engineering

This is to certify that I have examined this copy of a master's thesis by

Rıdvan Balamur

and have found that it is complete and satisfactory in all respects,

and that any and all revisions required by the final

examining committee have been made.

Committee Members:

_____

Assoc. Prof. Sedat Nizamoğlu (Advisor)

_____

Prof. Dr. Afsun Şahin

_____

Asst. Prof. Hasan Uluşan

Date: _____

ABSTRACT

Retina-Inspired Artificial Synapses and Near-Infrared Optoelectronic Neurostimulation Devices Using Quantum Dots

Rıdvan Balamur

Master of Science in Electrical and Electronics Engineering

August 12, 2024

Neurons are the building blocks of the nervous system and are responsible for generating, receiving, and transmitting electrical and chemical signals. By replicating the functionality of biological neurons, it is possible to achieve response capabilities that mimic human abilities. Such biomimetic signal generation and transmission at bio-electronic interfaces can restore, replace, or enhance biological functions. In addition, it can provide efficient event-driven processing and high-accuracy perception without separate memory and processing units. Neuromorphic bioelectronics, inspired by the functions of neurons, have the potential to enable biomimetic communication with cells. These systems necessitate operation in aqueous environments, generation of sufficient ionic currents for neurostimulation, and plasticity. In this thesis, a novel compact neuromorphic synapse is introduced, combining photodetection, memory, and neurostimulation functionalities within a single device. Utilizing cell-interfacing InP/ZnS quantum dots, this device achieves artificial photoreception through photo-faradaic charge-transfer mediated plasticity. The device induces excitatory post-synaptic currents that exhibit paired-pulse facilitation and post-tetanic potentiation in hippocampal neurons, simulating the natural biomimetic temporal summation of neuronal signals. Additionally, this thesis explores the potential of silver bismuth sulfide ($AgBiS_2$) colloidal nanocrystals for photovoltaic retina implants. $AgBiS_2$ nanocrystals, known for their chemical stability and absence of toxic heavy metals, have an exceptional absorption coefficient ($>10^5$ cm^{-1}) in the near-infrared (NIR) spectrum, surpassing silicon and many of inorganic nanocrystals such as PbS, CdTe, and perovskite. An ultrathin $AgBiS_2$ nanocrystal layer (24 nm) is integrated into a water-stable photovoltaic bioelectronic device, which produces high-level capacitive photocurrent (2.17 ± 0.2 $mA.cm^{-2}$) and ionic charge (10.97 ± 0.7 $\mu C.cm^{-2}$) in artificial cerebrospinal fluid. The long-term stability of the device and non-toxicity to neurons underscore its suitability for bioelectronic applications. Electrophysiological studies on primary hippocampal neurons reveal that these devices can elicit neuron firing at NIR intensity levels well within ocular safety limits. To sum up, this thesis demonstrated the first toxic heavy-metal-free nanocrystal-based optoelectronic biointerface operating within the NIR spectral window. Moreover, it shows that quantum dots hold high promise for unconventional and biomimetic control of cells for future retina implants.

ÖZETÇE

Kuantum Noktaları Kullanarak Retina İlhamlı Yapay Sinapslar ve Yakın Kızılötesi Optoelektronik Nörostimülasyon Cihazları

Rıdvan Balamur

Elektrik ve Elektronik Mühendisliği, Yüksek Lisans

12 Ağustos 2024

Nöronlar, sinir sisteminin yapı taşları olup elektriksel ve kimyasal sinyallerin üretilmesi, alınması ve iletilmesinden sorumludur. Biyomimetik sinyal üretimi ve biyolojik-elektronik ara yüzlerde iletimi, biyolojik işlevlerin geri kazanılmasını, değiştirilmesini veya geliştirilmesini sağlayabilir. Ayrıca, ayrı bellek ve işlem birimlerine ihtiyaç duymadan etkin olay yönlendirmeli işlem ve yüksek doğruluklu algılama sunabilir. Nöronların işlevlerinden ilham alınarak geliştirilen nöromorfik biyoelektronik, hücrelerle biyomimetik iletişim sağlamayı mümkün kılma potansiyeline sahiptir. Bu sistemler, sulu ortamlarda çalışma, nörositimülasyon için yeterli iyon akımlarının üretilmesi ve plastisite gerektirir. Bu tezde, foto-algılama, bellek ve nörositimülasyon işlevlerini tek bir cihazda birleştiren yeni bir kompakt nöromorfik sinaps tanıtılmaktadır. Hücre arayüzeyine sahip InP/ZnS kuantum noktaları kullanılarak, bu cihaz foto-faradaik yük-transferi aracılı plastisite ile yapay foto-soğurma sağlamaktadır. Cihaz, hipokampal nöronlarda, nöronal sinyallerin doğal biyomimetik zamansal toplamını simüle eden çift-darbe fasilitasyonu ve post-tetanik potansiyasyon gösteren uyarıcı post-sinaptik akımlar indüklemektedir. Ayrıca, bu tezde gümüş bizmut sülfat ($AgBiS_2$) kolloidal nano kristallerin fotovoltaik retina implantları için potansiyeli araştırılmaktadır. Kimyasal stabilitesi ve toksik ağır metalleri içermemesi ile bilinen $AgBiS_2$ nano kristalleri, silikon ve PbS, CdTe ve perovskit gibi birçok inorganik nano kristalden daha yüksek ($>10^5$ cm^{-1}) bir soğurma katsayısına sahiptir. Suya dayanıklı fotovoltaik bir biyoelektronik cihaza entegre edilen ince bir $AgBiS_2$ nano kristal tabakası (24 nm), yapay beyin-omurilik sıvısında yüksek seviyede kapasitif foto-akım (2.17 ± 0.2 $mA.cm^{-2}$) ve iyonik yük (10.97 ± 0.7 $\mu C.cm^{-2}$) üretmektedir. Cihazın uzun vadeli stabilitesi ve nöronlara toksik olmaması, biyoelektronik uygulamalar için uygunluğunu vurgulamaktadır. Birincil hipokampal nöronlar üzerindeki elektrofizyolojik çalışmalar, bu cihazların göz güvenliği sınırları içinde NIR yoğunluk seviyelerinde nöron ateşlemesini tetikleyebildiğini ortaya koymaktadır. Özetle, bu tez, NIR spektrumu penceresinde çalışan ilk toksik ağır metal içermeyen nano kristal tabanlı optoelektronik biyoarayüzü ortaya koymuştur. Ayrıca, kuantum noktalarının, gelecekteki retina implantları için hücrelerin geleneksel olmayan ve biyomimetik kontrolü konusunda yüksek bir vaatte bulunduğunu göstermektedir.

AKNOWLEDGEMENTS

I would like to express my thanks to my advisor, Assoc. Prof. Sedat Nizamoğlu for his tremendous support through my MSc study.

I would like to thank my thesis committee: Prof. Dr. Afsun Şahin and Asst. Prof. Hasan Uluşan for their helpful suggestions and valuable time. In addition, I would like to thank to the collaborators: Prof. Dr. Murat Hasanreisoğlu and Prof. Dr. Afsun Şahin, Prof. Gerasimos Konstantatos.

I thank to Dr. Baris Yagci and Dr. Amir Motallebzadeh from the Koc University Surface Science and Technology Center (KUYTAM). I gratefully acknowledge use of the services and facilities of the Koç University Research Center for Translational Medicine (KUTTAM), funded by the Republic of Turkey Ministry of Development.

The projects are funded by Scientific and Technological Research Council of Turkey (TUBITAK) with Project No 120E329, and the European Union (ERC, MESHOPTO, 101045289). Views and opinions expressed are however those of the author(s) only and do not necessarily reflect those of the European Union or the European Research Council Executive Agency.

I would like to thank my undergraduate supervisor Prof. Alper Erdoğan for his support and guidance through my undergraduate degree.

I am very lucky to meet all the current and former IDEALAB members: especially Onuralp Karatüm, Lokman Kaya, Asım Önal, Güncem Özgün Eren, Hümeyra Nur Kaleli, Tarık Safa Kaya, Ömer Faruk Özelci, Uğur Berkay Çalışkan. They not only were my colleagues, but they became my friends.

I would like to thank thank all my family members for their support through all my education.

I would like to extend my heartfelt gratitude to my friends, Enes Sefa Ayar, Adil Murat Çetinkaya, Ali Barbaros Küçüknane, and Seher Yüksel, for their unwavering support and companionship over the past decade. Your presence and friendship have been invaluable throughout this journey.

and my beloved wife, Melis: your love and support make me feel like the luckiest man alive every day.

TABLE OF CONTENTS

LIST OF TABLES

LIST OF FIGURES

ABBREVIATIONS

QD	Quantum Dot
QDAS	Quantum dot-based artificial synapse
NIR	Near-infrared
ECF	Extracellular fluid
aCSF	Artificial cerebrospinal fluid
PLL	Poly-L-Lsysine
CTG	CellTiter-Glo
OD	Optical density
SEM	Scanning electron microscopy
ITO	Indium tin oxide
PBS	Phosphate Buffered Saline
ETL	Electron transfer layer
HTL	hole transfer layers
EPSC	Excitatory post-synaptic current
PLQY	Photoluminescence quantum yield
HAD	Hexadecyl amine
MPA	3-mercaptopropionic acid
AP	Action Potential
AMD	Age-macular degeneration
NC	Nanocrystal
TMAI	Tetramethylammonium iodide
ZnO	Zinc oxide
P3HT	poly(3-hexylthiophene)
RuO_2	Ruthenium oxide
WE	Working electrode
RE	Reference electrode
CE	Counter electrode
CV	Cyclic voltammetry
EIS	Electrochemical impedance spectroscopy
LDH	Lactate dehydrogenase

Chapter 1:
INTRODUCTION

The nervous system is fundamental to drive vital biological processes like generation, reception, and transmission of electrical and chemical signals[1]. Using bio-electronic interfaces that can mimic the functionality of these biological neurons can lead to advancements in biomimetic signal generation and transmission which can enable the restoration, replacement, or enhancement of biological function[2-7]. This approach can also eliminate separate memory and processing units by providing efficient event-driven processing and high-accuracy perception[8]. Neuromorphic systems, which combine biological and synthetic components using organic synaptic transistors, have made significant progress in converting external signals like light, pressure, and sound into neuronal stimulation[9]. Unfortunately, the integration and efficiency of these systems are limited because they frequently need the serial connection of disparate components such as sensors, transistors, and stimulation electrodes.

Our first research presents a unique biohybrid neuromorphic device, a quantum dot-based artificial synapse (QDAS), that combines memory, photodetection, and neurostimulation features into all-in-one photovoltaic biointerface. The QDAS directly interfaces with neurons using InP/ZnS core/shell quantum dots (QDs) to generate a biohybrid synapse that facilitates short-term learning under light by eliciting excitatory post-synaptic currents via the Faradaic charge-transfer mechanism. This novel method mimics the temporal summation of living neurons, allowing neuron firing to be modulated with memory and showcasing the potential of nanomaterial-based synaptic biointerfaces for future neuroprosthetics and soft robotics.

Building on this foundation, our second study explores the field of photovoltaic neurostimulation devices for wireless communication with neurons. These devices present a method for controlling neuronal activity with the aim of converting light energy into neurostimulation. The objective of this work was to create an ultra-thin layer of $AgBiS_2$ nanocrystals to enable the development of an effective and capacitive near-infrared (NIR) stimulation device. $AgBiS_2$ nanocrystals have a very high absorption coefficient in the near-infrared spectrum and a narrow band gap. They are free of toxic heavy metals like lead or cadmium. The device functions without the need for wire

connections or external batteries, conveying large ionic photocurrents in biological media at low-intensity levels in the near-infrared range by integrating a nanoscale photoactive layer into a pin diode structure. This innovative device opens the door for safe and efficient retinal prosthesis and other neurostimulation applications with its stable functioning in physiological settings and excellent photostimulation of hippocampal neurons.

In summary, this thesis highlights the progress made in both photovoltaic neurostimulation and neuromorphic photostimulation, demonstrating the potential of nanomaterial-based biohybrid devices for unique neuroprosthetic solutions. The combination of various technologies into a single unit signifies a major advancement in the development of sophisticated neuromodulation devices that have the potential to improve the standard of living for those suffering from neurological diseases.

Chapter 2:
BACKGROUND

The history of bioelectricity dates back thousands of years, to the time of the ancient Egyptian and Greek cultures, who used the discharges of eels and catfish to improve blood circulation. However, there were very little improvement in the knowledge of bioelectricity util the term 'animal electricity' was first used in the late 18th century by Luigi Galvani. His work with frog legs demonstrated that electrical discharges cause muscle contractions. Further advancements came in the 19th century with the discovery of action potentials and the publication of seminal works in electrophysiology by Herman von Helmholtz and Emil Heinrich Du Bois-Reymond. Later in 1952, with the work by Alan Hodgkin and Andrew Huxley most famous computational biochemistry models were published on theory of the actional potential propagation in nervous system. An important breakthrough was made in the 1970s when Erwin Neher and Bert Sakmann developed patch-clamp techniques, which allowed for the comprehensive measurement of electrical activity in cells and set a standard for the field. Modern advancements in electrical neurostimulation owe a great deal to these historical advances.

Electrical neurostimulation is essential for understanding the nervous system and providing non-pharmacological treatments for neurological disorders. These devices can either stimulate or inhibit neural activity work by modulating membrane potential through electrical pulses. Over the years, number of these bioelectronic devices have been implanted in patients, treating a range of conditions such as heart failure, hearing loss, diabetes, and Parkinson's disease.

2.1 Mechanism of Electrical Stimulation

Electrical stimulation is a versatile and powerful tool for modulating neural activity with a wide range of applications in medicine and research. This stimulation method is a widely used for activating or modulating neural activity through the application of electrical voltage or current via electrodes. Typically, electrical stimulation employs a two-electrode configuration consisting of a working electrode and a counter electrode. The working electrode delivers the current to the target neural tissue, while the counter electrode completes the circuit, allowing current to flow through the system.

The extracellular fluid (ECF) between these electrodes plays a crucial role due to its ion-rich and conductive nature. The ECF is the electrolyte that facilitates the conduction of electrical currents and enables the transformation of charge carriers from electrons in the electrodes to ions in the fluid. This interaction creates an electric field across the neural tissue, which is fundamental for modulating neural activity. At the interface between the electrode and the electrolyte, a critical process occurs where electrons in the electrode interact with ions in the ECF, generating an electric field. This field induces electrical currents that changes the equilibrium of ions around neural membranes. As a result, the membrane potential of neurons changes, leading to either depolarization or hyperpolarization depending on the stimulation parameters. This alteration in membrane potential is essential for modulating neural activity, affecting how neurons fire and communicate.

However, electrical stimulation faces several challenges such as tissue damage from prolonged or intense stimulation, which can cause thermal effects, electrochemical byproducts, or inflammation. The invasiveness of electrode implantation also poses risks such as infection, and surgical complications. Additionally, the effectiveness of stimulation can be compromised by problems at the electrode-tissue interface, like corrosion or poor integration. Addressing these challenges is essential for enhancing the safety and efficacy of electrical stimulation, ensuring reliable neural modulation while minimizing adverse effects.

2.2 Optoelectronic Neurostimulation

In addition to traditional electrical stimulation, optoelectronic systems use light to induce changes in neural activity. These systems rely on exciton generation and dissociation, where light creates electron-hole pairs (excitons) that generate electric fields. These photogenerated carriers accumulate near the electrode/electrolyte interface, initiating electrochemical processes in the cellular environment. This process disrupts the distribution of ions such as sodium, potassium, and chloride near the neural membrane, leading to changes in neural activity similar to those caused by electrical stimulation.

The charge injection mechanisms at the electrode-electrolyte interface are influenced by the interfacial impedance, which might include both faradaic and capacitive processes. The faradaic mechanism involves redox reactions where electrons are transferred between

the electrode and ions in the electrolyte, leading to oxidation and reduction reactions that facilitate charge transfer. In contrast, the capacitive mechanism involves the charging and discharging of a double layer of ions at the electrode surface, without direct electron transfer, which reduces chemical reactions and potential tissue damage.

2.3 Neuromorphic Photostimulation

Neuromorphic devices for neurostimulation are also promising for advancing neural prosthetics by offering innovative solutions for restoring and enhancing neural function. These devices integrate principles from both electrical stimulation and neuromorphic engineering to create sophisticated systems capable of mimicking the natural dynamics of neural circuits. Unlike traditional stimulation methods, which rely primarily on electrical currents or light-induced excitons, neuromorphic neuroprosthetics utilize adaptive, bio-inspired technologies to deliver precise, context-sensitive stimulation. By leveraging the principles of neuromorphic engineering—such as mimicking the neural network's adaptive behavior and processing capabilities—these advanced prosthetics can modulate neural activity more effectively. The integration of neuromorphic devices into neuroprosthetics represents a significant step forward, providing more versatile and personalized options for restoring and enhancing neural function.

Chapter 3:
METHODS

Reproduced (adapted) from method section of Ref. [10] "Balamur, R., et al., A Retina-Inspired Optoelectronic Synapse Using Quantum Dots for Neuromorphic Photostimulation of Neurons. Advanced Science, 2024. ***11****(18): p. 2401753" and Ref. [64] "Balamur, R., et al., Capacitive and Efficient Near-Infrared Stimulation of Neurons via an Ultrathin $AgBiS_2$ Nanocrystal Layer. ACS Applied Materials & Interfaces, 2024".*

3.1 Biointerface Fabrication

Photoelectrodes were fabricated onto glass/ITO (Osilla, S111) and PET/ITO (Sigma-Aldrich). The substrate cleaning procedure consists of sonication in NaOH solution for 5 min, in tension-active agent mixed with deionized water solution (HELLMANEX II, 3%) for 15 min, in deionized water for 15 min, in pure acetone for 5 min, and finally in isopropyl alcohol for 5 min all at 55 °C. The cleaned substrates were treated with UV-ozone for 20 min to eliminate any other possible residues on the ITO surface.

For the bioelectronic interfaces with TiO_2 paste (Sigma-Aldrich) was diluted with ethanol 1:9 mass ratio and sonicated for 4 hours. Then, to obtain a more homogenous TiO_2 layer, 2 layer was coated by spin coating in 2000 rpm with 20 mins of 50°C annealing in between. After the second layer the substrates were annealed at 50°C for 5 mins, 100°C for 5 mins, 200°C for 5 mins, and at 400°C for 45 mins. QDs layer was coated on TiO_2 with layer-by-layer deposition. Each QD layer coating consists of 3 steps; first 50 $mg.ml^{-1}$ QDs in toluene were spined at 1000 rpm, then 1M 3-MPA methanol solution was coated with at 1000 rpm, the surface was washed with pure methanol by spin coating at 1000 rpm. After the desired thickness is obtained, the devices were annealed at 110°C for 10 mins. The thickness of the QD layers is characterized using cross-sectional SEM, Zeiss ultra plus field emission scanning microscope.

For ZnO layer coating, ZnO precursor solution was prepared by mixing 219.3 mg zinc acetate dehydrate ($Zn(CH_3CO_2)_2 \cdot 2H_2O$) from Sigma-Aldrich in 2ml of 2-methoxyethanol ($C_3H_8O_2$) and 90 mg of ethanolamine ($HOCH_2CH_2NH_2$) and sonicated for 25 min at 50 °C. Then, the ZnO solution was filtered by a 0.45 μm PVDF filter. ZnO

layer was spin coated onto the ITO substrates at 2000 rpm for 60 s and annealed at 280 °C for 20 min for glass and 200 °C for 1 hour for PET. Afterwards, three layers of $AgBiS_2$ NCs were deposited from 20 $mg.ml^{-1}$ toluene solution via the layer-by-layer method. For each $AgBiS_2$ NC layer, 50 µl of $AgBiS_2$ NC solution was spin coated onto ITO/ZnO substrates during spinning (2,000 r.p.m.). Then, TMAI/methanol (1% v/v) solution was applied to the NC film for 45 s, followed by two rinse– spin steps with methanol and once with toluene. The films were transferred into the glovebox for 10 min annealing at 115 °C. The P3HT (95.7% regioregular) (>99% pure, Ossilla) was utilized without any further purification. Photoactive solution was prepared as a 20 $mg.ml^{-1}$ solution of P3HT in o-dichlorobenzene, stirred for overnight at 70 °C. P3HT layer was fabricated onto ZnO layer by spin coating at 1500 rpm for 60 s and annealed at 150 °C for 10 min. For the characterizations and neuro-related experiments, biointerfaces that are fabricated on glass substrates were used.

3.2 Photo-electrochemical Measurements

The measurements were carried out using Olympus T2 upright microscope and EPC 800 patch clamp amplifiers (HEKA Elektronik GmbH, Pfalz, Germany). The modified artificial cerebrospinal fluid (aCSF) aqueous medium was prepared by mixing 10mM of 4-(2-hydroxyethyl) −1- piperazineethanesulfonic acid (HEPES), 10mM of glucose, 2mM $CaCl_2$, 140mM of NaCl, 1 mM of $MgCl_2$, 3mM of KC, and mixed with the distilled water. The pH was calibrated to 7.4 using 1M NaOH. As the illumination source, Thorlabs' blue (M450LP1) was used. LED system was driven by DC2200 - High-Power 1- Channel LED Driver with Pulse Modulation (Thorlabs Inc, NJ, USA). Photocurrent was measured without electrical grounding the ITO layer, and the ground is connected to the electrolyte solution to simulate the biological environment.

3.3 Preparation of Substrates for Primary Neuron Culture

Each substrate of the control ITO and the biointerfaces were rinsed with 70% ethanol before being left to dry out completely. Dried substrates were placed on the 6-well plates. Then, UV sterilization was carried out for 30 minutes under the cell culture hood. After the sterilization, substrates were coated with Poly-L-Lysine (PLL, Sigma-Aldrich, MO, USA) to increase cell attachment to the substrates for 4h in a 37 °C, 5% CO_2 cell culture

incubator. After incubation, the substrates were rinsed with Nanopure water and left to dry under culture hood before seeding the primary neurons.

3.4 Primary Neuron Isolation

All experimental procedures have been approved by the Institutional Animal Care and Use Committees of Koç University (Approval No: 2021.HADYEK.022) according to Directive 2010/63/EU of the European Parliament and of the Council on the Protection of Animals Used for Scientific Purposes. For isolation of primary hippocampal neurons, brains of Wistar Albino rats at embryonic day 15-17 (E15-E17) were dissected and blood vessel layer was removed carefully from brain. Cortexes were divided and hippocampi were dissected. Tissues were placed in ice-cold Hank's Balanced Salt Solution (HBSS, Thermo Fisher Scientific, MA, USA) supplemented with penicillin/streptomycin, glucose, and sucrose. After dissection, samples were washed twice with ice cold HBSS and they were incubated in 0.25% Trypsin-EDTA solution (Thermo Fisher Scientific, MA, USA) supplemented with 2% DNase-I (NeoFroxx, Einhausen, Germany) for enzymatic digestion for 20 minutes in a 37ºC water bath. After incubation, Dulbecco's Modified Eagle Medium/Nutrient Mixture F-12 (DMEM/F12 Thermo Fisher Scientific, MA, USA) supplemented with 10% fetal bovine serum (FBS, Heat Inactivated, GE Healthcare, IL, USA) and 1% penicillin/streptomycin (Thermo Fisher Scientific, MA, USA) was added to inhibit excess enzyme activity and tissue suspension was centrifuged for 3 min at 300 rcf. Supernatant was removed and plating Neurobasal Medium (NBM, Thermo Fisher Scientific, MA, USA) supplemented with B27, L-glutamine, penicillin/streptomycin, β-mercaptoethanol and glutamate was added on tissues. For complete digestion, tissues were triturate with a plastic Pasteur pipet for 10 times. Digested tissue suspension was passed through a 70 µm cell strainer. The homogenous cell solution was collected in new falcon tube, and they were cultured on poly-l-lysine (PLL, Sigma-Aldrich, MO, USA) coated ITO and Neuromorphic biointerfaces. Cells were incubated for 3 days at 37ºC incubator with 5% CO_2. After 3-day incubation, media was refreshed with NBM supplemented with cytosine arabinoside (Sigma-Aldrich, MO, USA) to eliminate glia proliferation. After 1-day incubation with glia inhibition media, fresh NBM was replaced to continue culturing for biocompatibility and electrophysiology experiments. Half of media were changed every 3-4 days.

3.5 Biocompatibility Assay

Cells' viability cultured on control ITO and NM devices was examined with CellTiter-Glo Viability Assay (CTG, Promega, Mannheim, Germany). After sterilization of the devices with 70% ethanol followed by UV irradiation for 30 min, substrates were placed in the 6-well plates and they were coated with poly-l-lysine (PLL, Sigma-Aldrich, MO, USA) solution prepared in ddH2O. Isolated primary hippocampal neurons were seeded as 500000 cells/well on PLL coated devices. After 3 days of incubation, AraC glia removal medium was added for 24 hours. After glia inhibition, fresh NBM was replaced to maintain culturing at 37 °C and 5% CO_2. Next day 1:1 ratio of CTG solution was added to cells cultured on substrates to check cell viability. Cells were incubated with CTG solution for 10 minutes at room temperature. The solution was transferred to 96-well opaque plate and the luminescence signals was measured with Synergy H1 Microplate Reader (Bio-Tek Instruments). The relative cell viability of each sample was calculated as follows: Viability = (ODsample/ODcontrol) × 100. The optical density (OD) of the sample was obtained from the cells grown on the photovoltaic substrates, and the OD of the control was obtained from the cells grown on the ITO control substrates.

3.6 Immunofluorescence Staining and Imaging

Primary hippocampal neurons were seeded as explained above on the ITO control and the Neuromorphic devices as 500000 cell/device. Short-term effect of samples on cell culture was checked at Day 0 and long-term alteration was monitored on Day 14. The neurons at Day 0 or Day 14 were fixed by cold 4% paraformaldehyde in PBS for 20 min and washed three times with PBS-T (Phosphate Buffered Saline, 0.1% Triton X-100). For permeabilization, the cells were incubated with 0.1% TritonX-100 in PBS for 8 min at room temperature. After permeabilization, cells were incubated with Superblock (Thermo Fisher Scientific, MA, USA) for 10 min at room temperature. For neuron characterization, mature neuron marker NeuN was used. For labelling of neurons, overnight incubation with anti-NeuN antibody (ab177487, Abcam, Cambridge, UK) in blocking solution was applied. After incubation, samples were washed with PBS-T and they were incubated with goat anti-rabbit IgG H&L Alexa Fluor 488 (Cell Signaling Technology, MA, USA) for 90 minutes at 37°C. To show morphology of neurons cultured substrates, they were labeled with FITC-conjugated phalloidin antibody for 90 minutes at 37°C. All samples

were washed three times with PBS-T, then mounted with DAPI supplemented mounting medium (50001, Ibidi GmbH, Germany). All immunofluorescence images were taken by inverted fluorescence microscope (Axio Observer Z1, ZEISS, Oberkochen, Germany).

3.7 Electrophysiology Experiments

Experiments were performed by EPC 800 patch clamp amplifier (HEKA Electronic GmbH, Pfalz, Germany). QDAS integrated and control devices were cleaned with 70 vol% ethanol solution and incubated for 3 days in DI water. The pulled patch pipettes of 4–6 MΩ were utilized to carry out the whole-cell patch clamp experiment. The internal cellular medium was prepared by mixing 140mM KCl, 2mM $MgCl_2$, 10mM HEPES, 10mM ethylene glycol-bis (β-aminoethyl ether)-N,N,N′,N′-tetraacetic acid (EGTA), 2mM Mg-ATP in water, and the pH was calibrated to 7.2–7.3 using 1M KOH. The intracellular solution was filled into the patch pipettes to achieve whole-cell patch. A digital camera integrated Olympus T2 upright microscope was used to patch and monitor the cells. LED system was driven by DC2200 - High-Power 1- Channel LED Driver (Thorlabs Inc., NJ, USA).

Chapter 4:

A RETINA-INSPIRED OPTOELECTRONIC SYNAPSE USING QUANTUM DOTS FOR NEUROMORPHIC PHOTOSTIMULATION OF NEURONS

Reproduced (adapted) from Ref. [10] Balamur, R., et al., A Retina-Inspired Optoelectronic Synapse Using Quantum Dots for Neuromorphic Photostimulation of Neurons. Advanced Science, 2024. ***11****(18): p. 2401753.*

Neurons are the building blocks of the nervous system and are responsible for generating, receiving, and transmitting electrical and chemical signals. They work in a fluid environment, communicate with synaptic transmission, and have plasticity via changing the strength of their response. By replicating the functionality of biological neurons, it is possible to achieve response capabilities that mimic human abilities [11]. Such biomimetic signal generation and transmission at bio-electronic interfaces can restore, replace, or enhance biological functions [12-15]. In addition, it can provide efficient event-driven processing and high-accuracy perception without separate memory and processing units [8, 16].

So far, neuromorphic conversion of exogenous signals (e.g., sound, pressure, light) into stimulation of neurons is achieved by bio-hybrid systems based on organic synaptic transistors, which advantageously offer biomimetic signal generation without bulky and rigid external encoding units [15]. These systems were used for tactile perception, vision-haptic fusion, and restoration of motion [13, 17-19]. They convert the external signals via an electronic sensor to electrical signals. Then, these electrical signals are applied to organic synaptic transistors for biomimetic plasticity. Finally, the output signals are applied to electrodes to stimulate neural tissues. However, such systems have been made of serial connections of separate elements such as sensors, transistors, and stimulation electrodes.

In this study, we introduce a novel biohybrid neuromorphic device, a quantum dot-based artificial synapse (QDAS), that combines photodetection, memory, and neurostimulation functionalities in a single compact device. QDAS employs InP/ZnS core/shell quantum dots (QDs), which directly interface with neurons and form a biohybrid synapse. The photovoltaic device elicits excitatory post-synaptic currents based

on the Faradaic charge-transfer mechanism facilitating short-term plasticity under illumination. This plastic photoresponse emulates the temporal summation of biological neurons and enables modulation of neuron firing with memory. These results demonstrate that synaptic biointerfaces based on nanomaterials can enable unconventional forms of neuromorphic devices for future neuroprosthetics and soft robotics.

4.1 Design of the quantum dot based artificial synapse (QDAS)

The concept of QDAS uses the direct conversion of light energy to neuromorphic ionic signals in the cellular environment for communication with neurons. All the light-to-ionic current conversion processes and neuromorphic signal generation are done by a single QDAS unit, which is analogous to the photoreceptor cells in the retina (Figure 4.1a). Biological photoreceptors absorb light and use neurotransmitters (i.e., glutamate) to convey information to secondary neurons (i.e., bipolar cells and horizontal cells). Secondary neurons communicate with the ganglion cells, which send action potentials to the brain via the optic nerve. In QDAS, light is absorbed by the InP/ZnS core/shell quantum dots, and the electron and hole pairs are mainly generated in the InP core (Figure 4.1b). The energy alignment facilitates tunneling of electrons through the ZnS shell and subsequently reaching the electron transfer layer (ETL) of TiO_2 and the conductive electrode of ITO (Figure 4.1c) [20]. The presence of a TiO_2 interlayer is crucial for facilitating an effective electron acceptor and transport layer, which is commonly used by previous reports (ETL) [20, 21]. The photogenerated holes can tunnel through the ZnS shell and become trapped in midgap states induced by the hole-acceptor MPA ligand [22-24]. Thus, the charge dissociation induces ionic photocurrent between the positive and negatively charged surfaces in an aqueous environment. The photovoltage on the quantum dots leads to a resistive (Faradaic) ionic photocurrent in the electrolyte, which is the postsynaptic current that induces action potentials by hippocampal neurons. Because of the Faradaic photoresponse, the neuromorphic signaling is triggered by the quantum dot and cell interface without any additional electrode. The photoactive side of the device acts as the stimulation electrode, and the ITO side acts as the return electrode that completes the current loop of the device-electrolyte circuit (Figure 4.1b). The flow of electric current between the QDAS and the cell leads to neurostimulation (Figure 4.1d).

Hence, the neuromorphic device is effectively coupled with the primary hippocampal neurons.

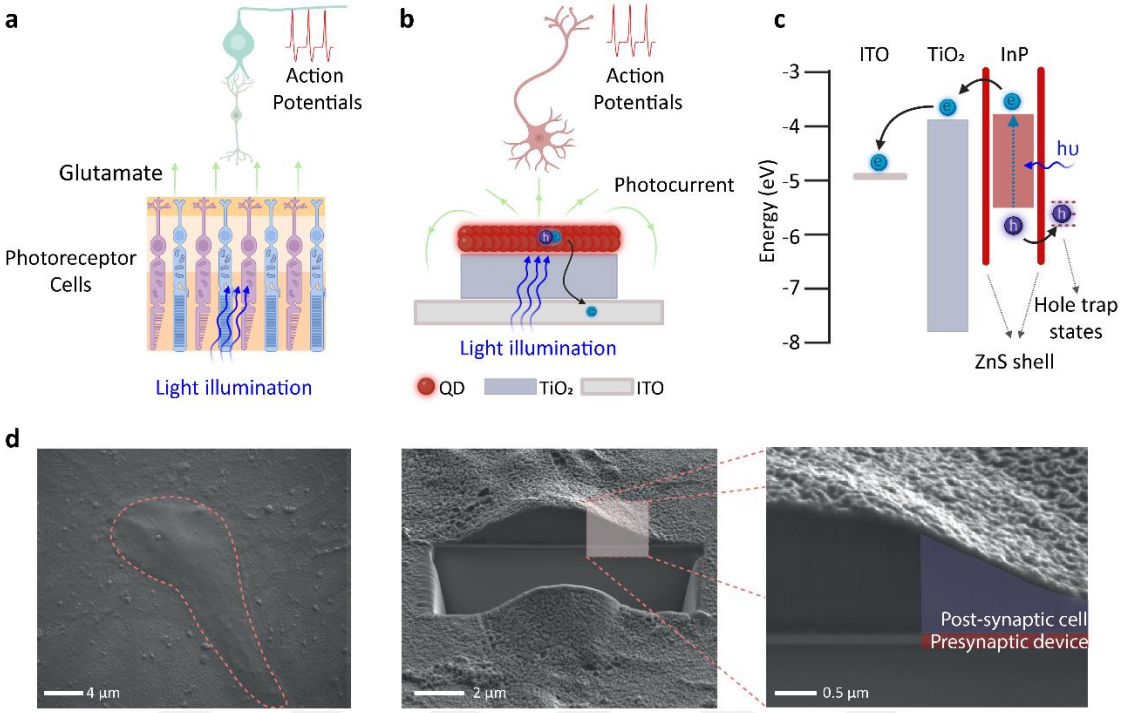

Figure 4.1 QDAS design and properties. a) Schematic comparison of working principle of photoreception by the retina and b) QDAS coupled with the hippocampal neurons. c) Energy band diagram of QDAS [56, 57]. d) SEM image of the (left) top view of the biointerface with the cultured hippocampal cells, (middle) FIB sectioned cell on the biointerface, and (right) QDAS (pre-synaptic device) coupled with the hippocampal neuron (post-synaptic cell).

4.2 Optimization photoresponse of QDAS

To emulate the excitatory post-synaptic current (EPSC) response of biological neurons, the lifetime of photocurrents needs to be at least in the milliseconds range [25]. Since the decay time of capacitive current due to double-layer capacitance is fast in sub-millisecond range [26, 27], Faradaic charge transfer is a suitable option that allows injection of ionic currents during the light turn-on periods and decays slowly in milliseconds range. In comparison with AlSb QDs generating capacitive currents [28], InP QDs are appropriate materials due to the Faradaic currents with longer lifetime [29-

31] and the three-electrode electrochemical characterization setup (in Figure 4.2a) is utilized to measure photocurrent characteristic of the QDAS.

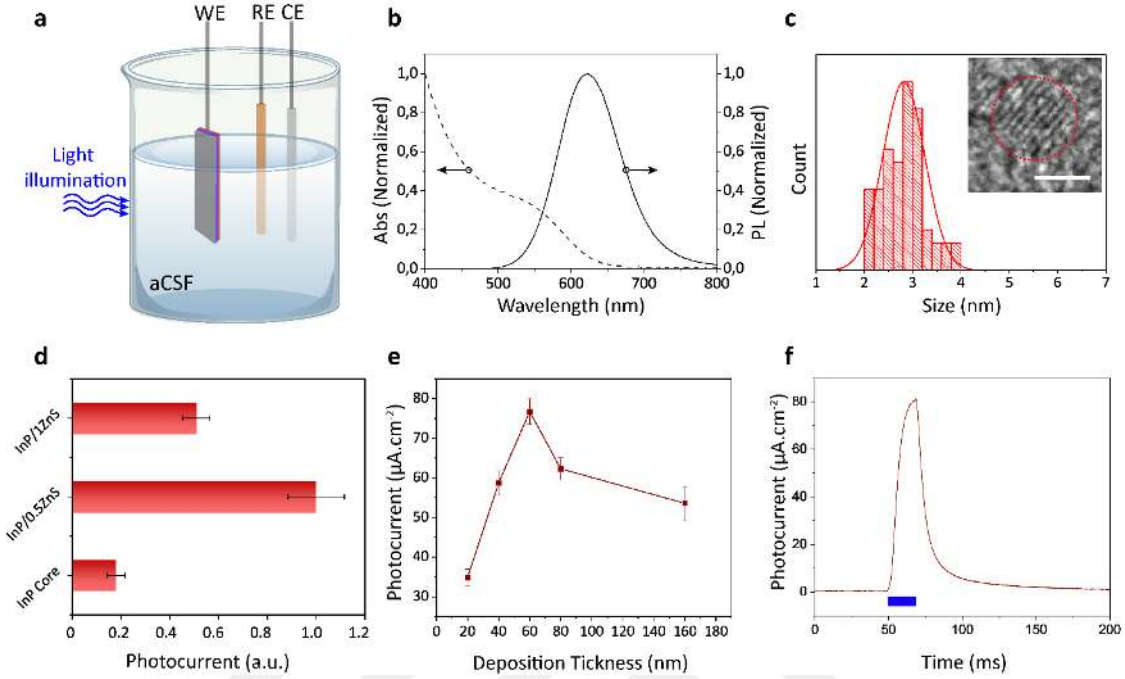

Figure 4.2 Photoelectrochemical characterization, optimization, and measurements. a) Schematic of photo-electrochemical setup. The setup included QDAS as the working electrode, a platinum counter electrode, and an Ag/AgCl reference electrode. Illumination was applied to the 1 cm^2 area of the device. b) Absorption and PL spectrum of InP/0.5ZnS core/shell QD. c) Size distribution of InP/0.5ZnS core/shell QDs. The inset shows the HR-TEM of InP/0.5ZnS. (Scale bar: 2 nm). 200 QDs are counted for size distribution. d) Photocurrent response of InP core, InP/0.5ZnS, and InP/1ZnS core/shell QDs (The error bars indicate the deviation in results from three distinct QD syntheses). e) Photocurrent response of QDAS with InP/0.5ZnS core/shell QDs for different QD layer thicknesses. The photocurrent is measured under 450 nm light pulses with 20 ms pulse duration (means ± SD, n=5). f) Photocurrent response of optimized QDAS under 20 ms, 450 nm light illumination.

InP core quantum dots (QDs) were synthesized using an amine-derived synthetic approach, with a mean size of 2.49 nm [32]. A 0.16 nm thick ZnS shell, corresponding to 0.51 monolayers, was grown on top of the InP core using successive ionic layer adsorption and reaction (SILAR) method to investigate the effect of the shell on the photocurrent [33-35]. The InP/0.5ZnS QDs have a cubic crystal structure, and their photoluminescence is in the red spectral region (Figure 4.2b, c). The shell growth reduces

trap states, which is evident from the increase in the photoluminescence quantum yield (PLQY) from 10.7% to 16.1%. Compared to InP core QDs, InP/0.5ZnS core/shell QDs exhibit a significant enhancement in photocurrent peak (Figure 4.2d). However, when the ZnS shell thickness is further increased to 0.33 nm (Figure 4.3), corresponding to 1.05 monolayers (i.e., InP/1ZnS), the photocurrent peak starts to drop. This is due to the decrease in the tunneling probability of photogenerated charges by the thicker potential barrier of ZnS, which also affects the rise and fall time of the photocurrent.

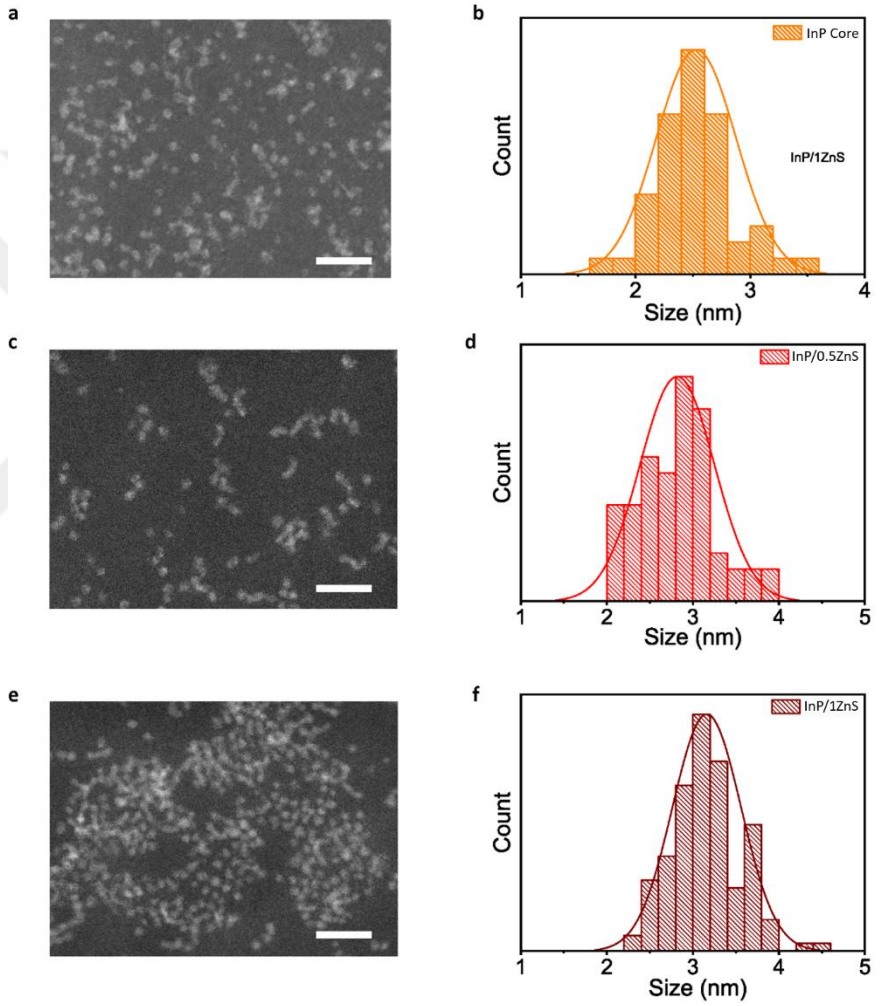

Figure 4.3 a) TEM image of InP core QDs. b) Size distribution of InP core QDs where the mean size is 2.49 nm. c) TEM image of InP/0.5ZnS core/shell QDs. d) Size distribution of InP/0.5ZnS core/shell QDs where the mean size is 2.81 nm. e) TEM image of InP/1ZnS core/shell QDs. f) Size distribution of InP/3ZnS core/shell QDs where the mean size is 3.15 nm. 200 QDs are counted for each size distribution plot. Scale bars of TEM images are 20 nm.

Thus, we analyzed the rise and fall time for different shell thicknesses. For the InP core QDs, we observe a shorter fall and rise time in comparison with the InP quantum dots with ZnS shell (Figure 4.4). Here, the difference stems from the fact that the ZnS shell forms a potential barrier that limits the tunneling of the photogenerated charges. Hence, when the shell thickness increases, both the fall and rise times increase. If we look at the difference between the rise and fall time, the ratio of the fall to rise time increase when the shell thickness increases. We attribute this to the fact that detrapping of the holes from the surface states slows down the recombination process. Hence, we select to use InP/0.5ZnS core/shell QDs for QDAS since they produce higher photocurrent with favorable rise/fall time ratio.

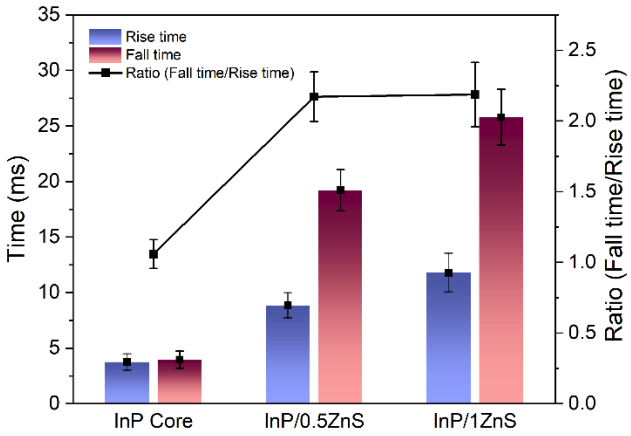

Figure 4.4 Rise time, fall time, fall time/rise time analysis of the QDAP devices with different QD nanostructures.

To achieve reduced interparticle spacing for high conductivity and colloidal stability of the QD film in aqueous environments, the large native ligands of hexadecylamine (HDA) are replaced with the short-chain ligand of 3-mercaptopropionic acid (MPA) via solid-state ligand exchange. After QDs are coated on the TiO_2, the process involves using spin-coating of QDs, soaking to the solution with MPA for ligand exchange and washing with protic solvent to remove excess new short ligands. MPA also functions as a hole acceptor on the QD surface, which is beneficial for the photovoltaic effect that can induce potential difference between working and return electrodes for photocurrent generation [23]. Different QD layer thicknesses are investigated to understand the photocurrent levels in artificial cerebrospinal fluid, which is close to the condition of the cellular environments (Figure 4.2e). If the photoactive layer is thick, extracted charges recombine

in the neutral region, which decreases the charge extraction efficiency. On the other hand, thin photoactive layer is disadvantageous due to low absorption [36, 37]. We obtained the maximum photocurrent when the QDs layer thickness is 60 nm. A single spike of light illumination can trigger an EPSC of 80 $\mu A.cm^{-2}$ (Figure 4.2f), and EPSC decays to the baseline level within tens of milliseconds because of the surface-voltage drop after recombination and discharge through the return electrode.

To understand the source of photocurrent, we did electrochemical analysis of QDAS in aCSF solution by removing the ingredients one by one. We observed that when HEPES is removed, the photocurrent significantly decrease, and this shows that HEPES oxidation is an essential enabler for Faradaic photocurrent generation (Figure 4.5) [38]. As a control, we removed QDAS, and when we measured the photocurrent of only TiO_2-coated ITO devices, no detectable photocurrent was observed, indicating that the HEPES photooxidation process was triggered by QDAS. Therefore, water [39] and HEPES oxidations by QDAS are possible sources of electrochemical photocurrent.

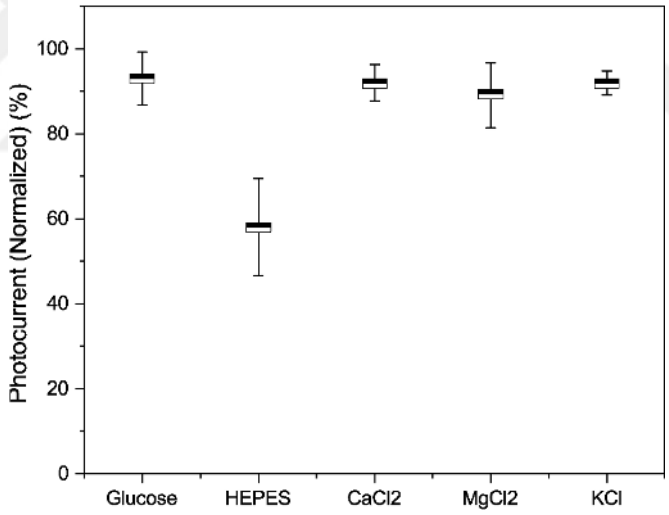

Figure 4.5 Photocurrents while each ingredient is decreased to their half (means ± SD, n=5).

4.3 Synaptic characteristics of QDAS

In biological neurons, the action potentials of presynapse trigger the release of the neurotransmitters across the synaptic cleft and lead to the generation of action potential in the post-synapse with plasticity. Likewise, the light pulses induce the accumulation of holes on the device surface, and the positive photovoltage by the neuromorphic device leads to a postsynaptic Faradaic current for neurostimulation with short-term memory.

When subsequent inputs are applied to the QDAS, the charges cannot find sufficient time to discharge across the return electrode, and the amplification of the EPSC is observed (Figure 4.6a). The amplitude of EPSC from the second spike (A_2) is almost doubled with respect to the first spike (A_1), and the EPSC saturates to a level of 40 $\mu A.cm^{-2}$ after eight spikes. This accumulation of EPSC signals can be modulated by changing the illumination frequency. When the illumination frequency increases from 5 to 100 Hz, the amplification of EPSC signals increases from 19 $\mu A.cm^{-2}$ to 100 $\mu A.cm^{-2}$, respectively (Figure 4.6b). Each applied pulse for different frequencies has 5 ms on time and frequency depends only on off-time of the illumination. Therefore, the saturation level depends on the duration of the off-time, where longer durations will cause more relaxation of photocurrent, and cause lower saturation current for that specific frequency. Such amplified signal generation is also observed by biological neurons in the hippocampus, cortex, and spinal cord [40, 41].

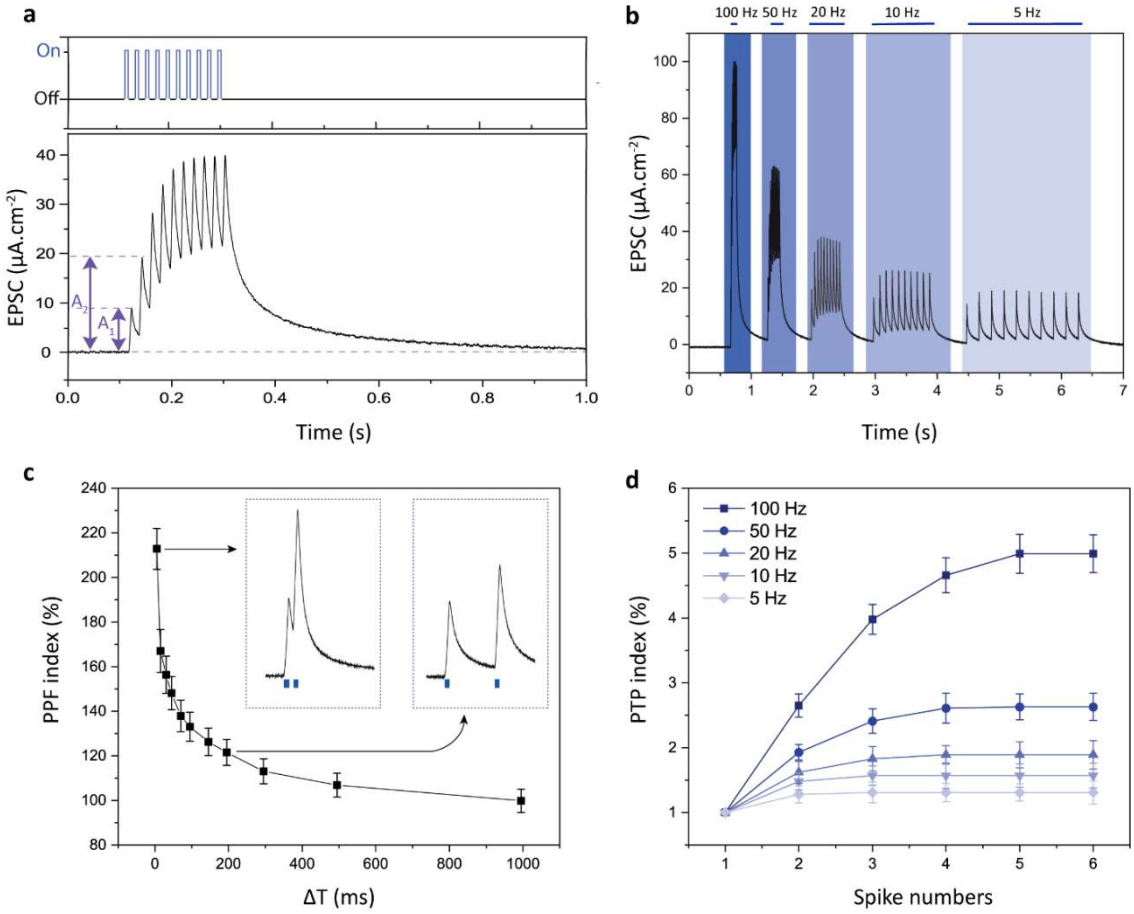

Figure 4.6 Photo synaptic characterization of QDAS. a) (Top) The applied illumination pulse train and (bottom) the resulting EPSC. b) EPSC under light pulse train consisting of ten spikes with frequencies of 100, 50, 20, 10, and 5 Hz (from left to right) (off time:

5, 15, 45, 95, 195 ms, respectively, and on time: 5 ms). c) PPF index (%) is defined as 100% × A_2/A_1 for different off-times (ΔT). The on-time is 5 ms. The left inset shows EPSC with ΔT=5 ms, and the right inset shows ΔT=195 ms. d) PTP index (%), defined as 100% × A_n/A_1, is plotted as a function of the number of spikes (n = 1:6) for different frequencies. A_n and A_1 represent the amplitudes of the n^{th} and first pulses, respectively. The on-time is 5 ms.

The PPF index measures the short-term plasticity depending on the applied input, and similar to biological neurons, QDAS displays stronger PPF index when two consecutive spikes are applied with smaller off times (Figure 4.6c). For example, while the pulses with the off-time of 195 ms are applied, the accumulation of photocurrent leads to a PPF of 121%, and if the off-time decreases to 5 ms, PPF increases to 213%. The PTP index was also investigated for different frequencies (Figure 4.6d), and the PTP index increases with the higher frequency illumination trains. For example, while the PTP index is 131% at 5 Hz illumination, it can reach up to ~500% at 100 Hz. High-frequency action potential firing elevates the synaptic strength of biological neurons, and analogously QDAS also increases the photocurrent response in high-frequency bursts of light illumination.

4.4 Biocompatibility

Biocompatibility is an important need for biointerfacing with neurons, and the composition of cell interfacing QDs directly affects biocompatibility. Brain cells, especially in the hippocampal region, are cell populations widely used in electrophysiology studies and allow the evaluation of action potential abilities in different conditions. If the devices would induce toxicity on cells, the stress on neurons would be decremental on electrophysiology. Herein, we used hippocampal neurons isolated from rat embryos at embryonic days 15-17 for cell culture and patch clamp experiments. The neurons were cultured on QDAS and ITO control substrates for viability and morphology analyses to examine the short-term effect after 3-days of incubation. On 3-days of cell culture, a slight reduction of cell viability was observed on QDAS substrates compared to the control substrates (Figure 4.7a). In terms of inorganic nanostructure, the ZnS shell has non-toxic elements, leading to even high biocompatibility for cadmium-based quantum dots [42, 43]. Here we consider that the slight decrease of biocompatibility may

be due to TiO_2 [44-46]. Cytoskeleton and adult neuron marker stainings were performed on day 14 of culture to check long-term cell characteristics and morphology changes. Cells were fixed after 3-day and 14-day cultures and stained with NeuN and f-actin filaments to visualize nucleus, cytoskeletal and network connections. According to the results, cells can establish enhanced neurite connections on neuromorphic devices as on control substrates and adapt to the long-term culture condition (Figure 4.7b). Before performing electrophysiology experiments, we checked the stability of the device after 14 days in culture environment (Figure 4.7c) and observed sufficiently high-level of photocurrents, 80% of the initial photocurrent level, for neurostimulation.

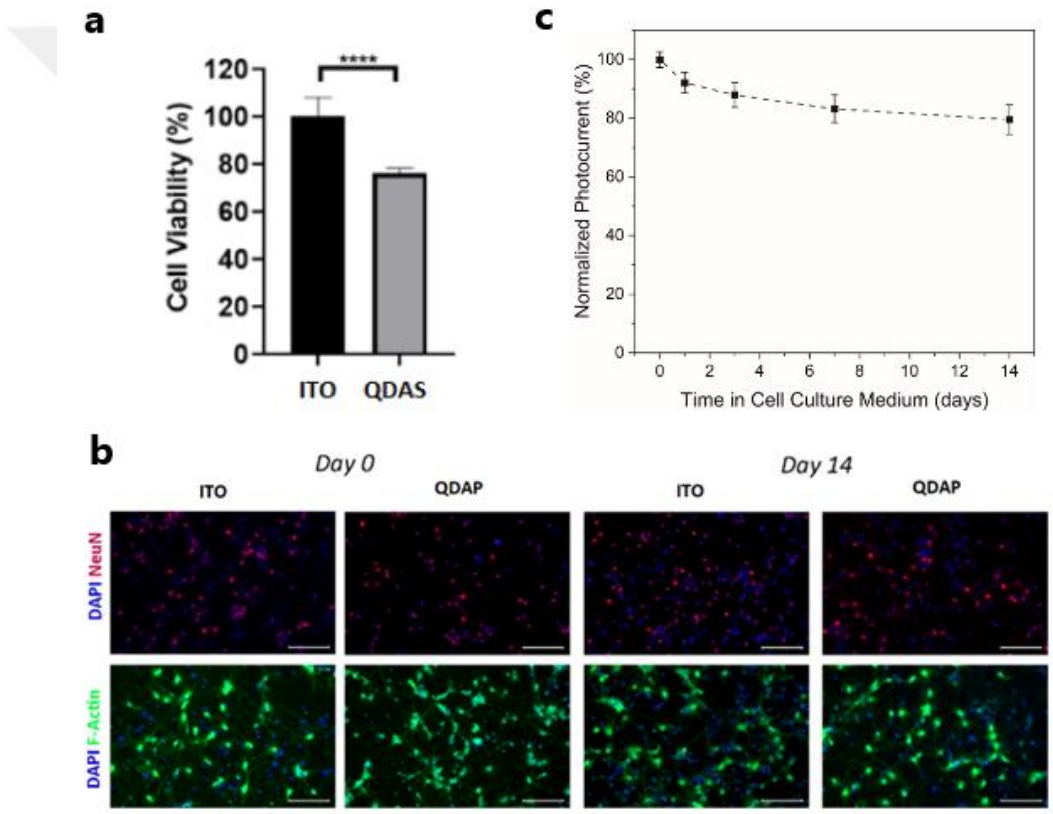

Figure 4.7 a) Biocompatibility analysis of QDAP compared to ITO control. CTG cell viability result of primary hippocampal neurons cultured on QDAPs and ITO substrates (mean ± SD for n = 4). An unpaired, two-tailed t-test was used for statistical analysis, and ****$p < 0.0001$ was evaluated as statistically significant. b) Immunofluorescence images of primary hippocampal neurons cultured on QDAP and ITO substrates on days 0 and 14 of culturing to observe morphology and viability of primary hippocampal neurons. Cells were co-stained with DAPI (blue) to show the nucleus, Anti-NeuN (red) to show the

neuronal nucleus, and Anti-f-Actin (green) to indicate cell structure (scale bar: 100 μm). c) Normalized Photocurrent peak up to 14 days of cell culture.

4.5 Biohybrid neurostimulation

For biohybridization, we cultured primary hippocampal neurons on the synaptic device. To investigate the coupling of the neuromorphic device with biological neurons, we used patch clamp electrophysiology to record the single-cell electrical activity under illumination (Figure 4.9a). The intracellular potential of the cultured cell is measured from the cell soma (Figure 4.9a inset) with respect to a distant Ag/AgCl bath electrode in the whole-cell configuration without applying any bias current during the measurements. The cells show a mean resting membrane potential of -65 mV, and cells can go into a non-linear response as an action potential (AP) with a depolarization of 25 mV (Figure 4.9b).

To show the coupling of synaptic plasticity to the biological neurons, we use light signal configurations in milliseconds time scale, compatible with the electrophysiological activity of neurons. Each light signal configuration is composed of five successive light pulses with varying on- and off-times (i.e., x_y where x is the on-time and y is the off-time in milliseconds) and transduces clearly observable EPSC peaks for each light turn-on period (Figure 4.9c). When QDAS is repeatedly stimulated within a short time period, the inputs add up over time, mimicking temporal summation by biological neurons (Figure 4.9d) [47]. The summation was achieved by flashing light on the neuron with a repetition period shorter than the decay time, which is not possible via currents due to double-layer capacitance (Figure *4.8*). While the condition of light pulse configuration changes from 2_5 to 5_5 and 5_2, the peaks and the total charges generated by the EPSC increase because of the biomimetic response.

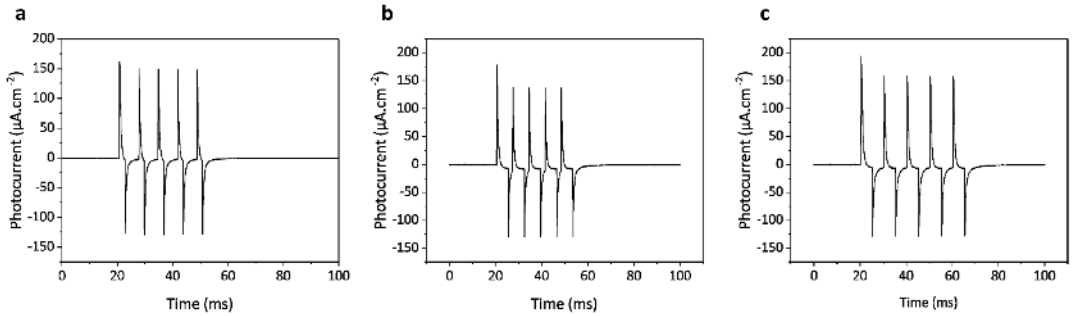

Figure 4.8 Capacitive photocurrent response of ITO/ZnO/P3HT device triggered with different illuminations, (a) illuminated with 2 ms on time and 5 ms off time, (b) illuminated with 5 ms on time and 5 ms off time, (c) illuminated with 5 ms on time and 2 ms off time.

Since the surface charge of the QDAS is positive under illumination due to the confinement of the photogenerated holes, QDAS induces EPSC from the QD surface toward the electrolyte that induces hyperpolarization of the attached membrane and depolarization of the recorded free membrane [48] (Figure 4.9e, f). Like in EPSC, the depolarization peaks of the membrane potential are also observable after each flash of light (Figure 4.9e). For the light signal configuration of 2_5, the membrane can only depolarize 13-mV after five successive light pulses (Figure 4.9e, top)) and thus, the probability of obtaining action potential is low, which is 15% (Figure 4.9g and f, top)). Increasing the on-time to 5 ms while keeping the off-time fixed at 5 ms (i.e., 5_5) strengthened the EPSC signal (Figure 4.9c, middle) and increased the depolarization in the membrane potential (Figure 4.9e, middle). Thus, the probability of generating an action potential significantly increased to 75% (Figure 4.9f, middle and 4.9g)). To further boost the EPSC signal, the off-time is reduced to 2 ms while maintaining the on-time constant at 5 ms (i.e., 5_2) (Figure 4.9c bottom), and this pulse configuration was able to produce action potentials with a probability of 90% (Figure *4.9*e and 4.9f bottom, 4.9g). A glass/ITO substrate was employed as a control device, and there was no depolarization or action potential production with the light irradiation on the control device. Moreover, the light intensity level (30 $mW.cm^{-2}$) is advantageously below the ocular safety limits [49].

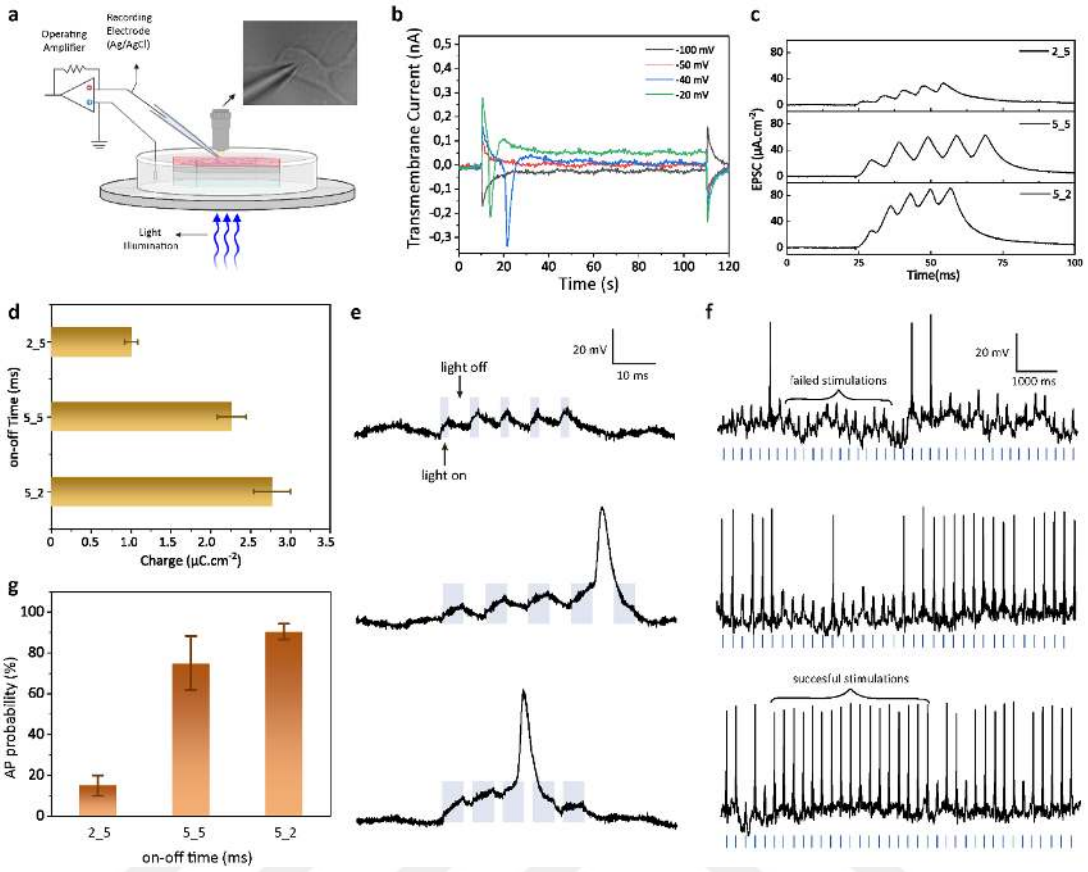

Figure 4.9 Single cell electrophysiology recordings of QDAS. a) Schematic of the patch-clamp electrophysiology recording setup. The inset shows a photograph of an exemplary patched hippocampal neuron. b) Recorded transmembrane currents in whole-cell configuration for different holding potentials. c) Probability of generating action potential (AP) for different on and off cycles (mean ± SEM, n=3). d) EPSC signal triggered with different illuminations, (top) illuminated with 2 ms on-time and 5 ms off-time, (middle) illuminated with 5 ms on-time and 5 ms off-time, (bottom) illuminated with 5 ms on-time and 2 ms off-time. e) Photogenerated charge with different illumination on-off cycles calculated from (d). f) Membrane potential under a single light signal. The signal consists of five successive pulses with varying on- and off-times (x_y). g) Membrane potential under the light train of the signals in (f) at a frequency of 5 Hz. The top, middle, and bottom panels correspond to x_y values of 2_5, 5_5, and 5_2, respectively, where x and y denote the on- and off-times in milliseconds.

The QDAS's compactness and wireless operation make it advantageous for implantation into vulnerable tissues. The use of wires and interconnected receiving and processing electronics during surgery can be a significant source of difficulty and may

lead to unwanted side effects [50]. Previous studies have shown that photovoltaic retinal implants can be implanted into the sub-retina [51] and epi-retina [52], demonstrating the potential of photovoltaic devices for implantation. Compared to wired systems such as Argus II and Alpha AMS, which require 4 hours of surgery time, PRIMA without any wires can be implanted in 1-2 hours [53]. Hence, compact, and wireless devices hold high promise for future neuroprosthetics.

Sufficiently high level of charges is generated for neurostimulation because of the Faradaic nature of the current. Even though the capacitive currents are the preferred way of stimulating neurons for clinical application, electrochemical currents have been utilized for neuronal excitation in previous studies [27, 54, 55] and we also observed precise and repetitive firing of neurons. The transparency of the eye is advantageous for generating sufficiently strong photocurrent levels in the retina by direct illumination of external light sources. In addition, injection of the achievable charge levels by QDAS in the range of tens of $\mu C.cm^{-2}$ can facilitate stimulation of a wide variety of tissues, including the sciatic nerve, subthalamic nucleus, and cortical neurons [55-57]. Moreover, biocompatible optical fibers can be used to deliver light to the QDAS when it is implanted into non-transparent parts of the body [58-60].

Biomimetic neurostimulation devices can be combined with artificial sensing [61] and spiking neurons [62, 63] to develop advanced neuromorphic systems. Previously, electrochemical transistors were used to sense neurotransmitters such as dopamine and regulate synaptic plasticity through channel conductance variation [61]. These transistors also enabled the development of neuron-like spiking circuits controlled by ion concentration [15, 61]. Combining ionic sensing, spiking, and receiving actuation signals (e.g., light, sound, and motion) with neurostimulation can lead to organ-like closed-loop neuromorphic systems. This strategy can be beneficially used for future neuroprosthetics and miniaturized robots to rehabilitate neurological disorders.

In conclusion, we showed that cell-interfacing quantum dots enabled photon detection, synaptic and neurostimulation functionalities in one single compact device architecture. The device imitated the short-term plasticity of biological neurons via Faradaic currents and converted light pulses to neuromorphic photostimulation of neurons. Hence, nanomaterials show high promise as a building block for unconventional and biomimetic control of cells.

Chapter 5:

CAPACITIVE AND EFFICIENT NEAR-INFRARED STIMULATION OF NEURONS VIA ULTRA-THIN $AGBIS_2$ NANOCRYSTAL LAYER

Reproduced (adapted) from Ref. [64] Balamur, R., et al., Capacitive and Efficient Near-Infrared Stimulation of Neurons via an Ultrathin $AgBiS_2$ Nanocrystal Layer. ACS Applied Materials & Interfaces, 2024.

Electrical neurostimulation plays a crucial role in unraveling the mysteries of the nervous system and offering drugless treatments of neurological diseases[2]. These devices operate by extracellular modulation of membrane potential through electrical pulses, which either activate or silence neural activity. In this process, an implantable pulse generator sends electronic signals via lead wires to the electrodes, inducing ionic currents that traverse through nerve tissue back to the return electrode[65]. Over the years, millions of such bioelectronic devices have been successfully implanted in patients, enabling the treatment of diverse conditions including heart failure[3], hearing loss[4], diabetes[66], and Parkinson's disease[5].

Next-generation neurostimulation devices aim for wireless communication with nervous system[67]. Among a wide variety of energy transfer options such as ultra-sound, radio-frequency, temporal interference, light allows wireless transfer of energy with high spatial and temporal resolution[68, 69]. Hence, photovoltaic biointerfaces that convert light energy to neurostimulation (i.e., photostimulation) emerged as an exciting approach for the control of neural activity[70]. They have been used to stimulate a wide range of nerve tissues such as motor cortex[27], sciatic nerve[71], heart[55, 72, 73] and retina[52]. Even, in the clinical level they stimulate the retinal tissue and enable enhanced visual acuity for the patients with age-macular degeneration (AMD)[74]. In the implants silicon photodiodes are used and they convert the near-infrared (NIR) radiation to photovoltage to bias the electrodes[75]. They operate in the NIR window to directly communicate with the implant without any crosstalk with the surviving photoreceptors, however, the low absorption coefficient of silicon in NIR window (e.g., 383 cm^{-1} at 880 nm) demands thick photoactive region (30 µm) making rigid implants[76].

Colloidal nanocrystals (NCs), which have inorganic crystal structures like silicon and solution-processability like polymers, show high promise for flexible bioelectronics. They offer unique features such as tunable electronic energy levels via quantum confinement effect, surface engineering via ligand exchange, and high-level of compositional variations[31]. For neuromodulation, NCs such as CdSe, CdS, InP and AlSb have been used for photostimulation of neurons that operate within the visible range[28, 77-79]. Alternatively, HgTe NCs show favorable photoresponse up to near-infrared spectral range but they are coupled with neurons via a Faradaic pathway[80] that may lead to unwanted pH change of cellular environment[81]. Instead, PbS NCs have demonstrated their ability to induce safe capacitive coupling with neurons[82]. However, the destabilization of the quantum dots could potentially result in the diffusion of lead species into body[83], which raises concerns about their translation to clinical devices[84].

In this study, we demonstrate $AgBiS_2$ NCs, which do not have any toxic heavy metal content such as cadmium or lead, for efficient and capacitive photovoltaic neurostimulation in NIR. We selected $AgBiS_2$ NCs because of their relatively narrow band gap (1.1 eV), and remarkably their absorption coefficient can reach over 10^5 cm^{-1} in NIR that is stronger than other NCs such as PbS, CdTe, perovskite, etc. and approximately 2-orders of magnitude higher than silicon[85]. Thanks to their exceptional photoabsorption strength, we integrated a nanoscale photoactive layer into a pin diode structure that transduced high ionic photocurrents in biological medium at low-intensity levels in NIR. The devices operate without any wire connection or external battery and maintain stability in physiological conditions without any toxicity on cells. The device triggers capacitive and efficacious photostimulation of hippocampal neurons significantly below the ocular safety limits. This study reports the first toxic-heavy-metal-free nanocrystal based optoelectronic biointerfaces operating in NIR paving the way toward retinal prosthetics.

5.1 Bioelectronic device and characteristics

The photovoltaic bioelectronic device consists of two parts: stimulation and return electrodes (Figure 5.2a). We synthesized $AgBiS_2$ NCs, and the stimulation electrode was fabricated by using a thin $AgBiS_2$ NC layer (24 nm) (Figure 5.2b and c). NCs have oleic

acid as the native ligands, but these long chains hinder efficient device production due to poor conduction. Because of that, oleic acid ligands were exchanged with tetramethylammonium iodide (TMAI)[86]. This passivation, involving stronger Bi-I and Bi-S bonds, enhanced stability, electronic properties, and performance, which led to ~10-fold increase of photocurrent (Figure *5.1*). The energy band alignment indicates that NIR-absorbing $AgBiS_2$ NCs are promising candidates to form proper heterojunction between ZnO and P3HT layers (Figure 5.2c and d)[26, 86, 87]. We integrated this photoactive layer between a 29 nm layer of zinc oxide (ZnO) and 47-nm poly(3-hexylthiophene) (P3HT) to promote effective exciton dissociation, and photovoltage generation between the stimulation and return electrodes (Figure 5.2d).

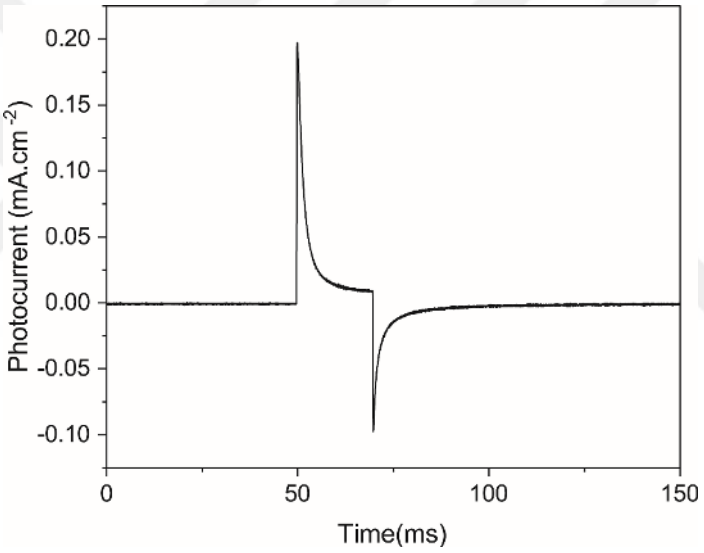

Figure 5.1 Photocurrent of the biointerface without applying the TMAI treatment. The biointerface has the following structure: ITO/ZnO/AgBiS2/P3HT with RuO2 in the return electrode. Illumination condition: 20 ms, 780 nm, 0.5 mW.mm-2.

The return electrode is formed via electrochemical deposition of ruthenium oxide (RuO_2) on indium tin oxide (ITO), which can generate capacitive photocurrent[88]. Hence, the bioelectronic device consisting of ITO/ZnO/$AgBiS_2$/P3HT (stimulation), and ITO/RuO_2 (return) electrode completes the Kirchhoff's current loop with the electrolyte. Advantageously, the complete device is flexible because of the hundreds of nanometers thick total device thickness (Figure 5.2b). To investigate the performance metrics of the photodiode, we added contact electrode MoOx (3nm) / Ag (120nm), and the IV characteristics show that the photovoltaic device works properly with an open-circuit

voltage of 0.34 V and short-circuit current of 9.24 $mA.cm^{-2}$ under 1-sun illumination (Figure 5.2f). The EQE of the device is 19.81% at 780 nm and a responsivity of 0.12 A/W (Figure 5.2g).

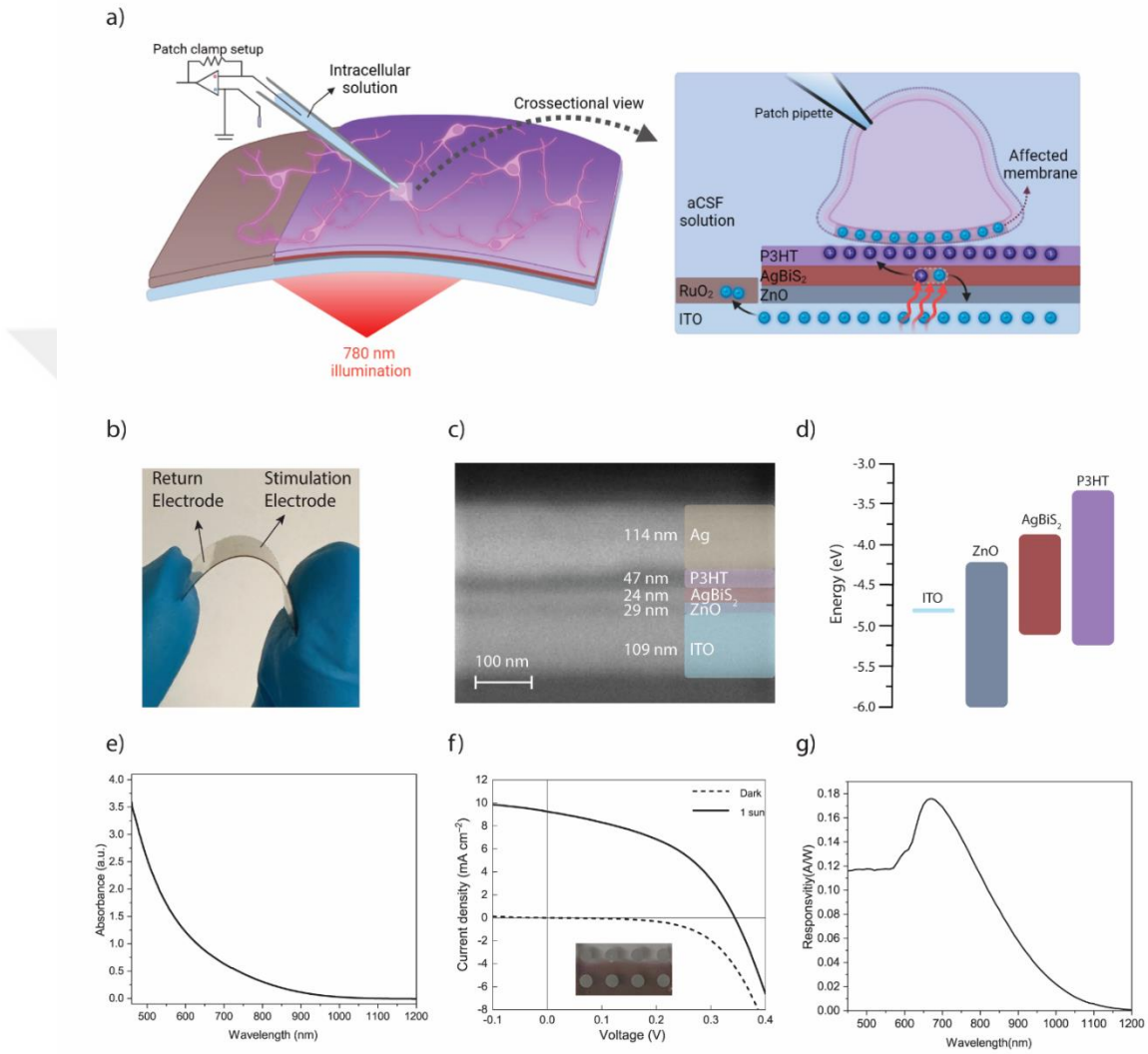

Figure 5.2 a) Schematic of biointerface with cells cultured on top (not to scale) (left). Patch clamp electrophysiology is employed to assess the electrical activity of the cell membrane under whole cell configuration. The cross-sectional view of the coupling of biointerface with the adjacent cell (right). The stimulation electrode is composed of the ITO/ZnO/$AgBiS_2$/P3HT layers, and the return electrode is made of electro-chemically deposited RuO_2 layer on ITO. b) Photograph of the flexible bioelectronic device on PET/ITO substrate. c) Cross-sectional FE-SEM image of the biointerface. The MoOx/Ag layer is added for electrical characterization of the photodiode. d) Energy band diagram of the photodiode. e) Absorbance of the $AgBiS_2$ NCs. f) J-V of the photodiode coated

with MoOx/Ag as the contact electrode under dark and 1-sun illumination condition. g) Responsivity of the photodiode for different wavelengths.

5.2 Biointerface operation and photo-electrochemical characterization

The operation of the biointerface begins with the absorption of NIR light by the $AgBiS_2$ NC layer. The absorption of light results in the generation of electron and hole pairs, and then they disassociate because of the band alignment and transferred to the electron transfer (ETL) and hole transfer layers (HTL). The electrons migrate toward the lower energy states in the ZnO and then move to the conductive ITO layer. Eventually, the electrons that are transferred into the ITO move to the RuO_2 layer, which has a high electrochemical surface area/geometrical surface area (ESA/GSA) ratio that provides high interfacial capacitance[88]. On the contrary, the holes move to the lower hole energy states toward P3HT.

Three-electrode setup with an artificial cerebrospinal medium (aCSF) is used for photoelectrochemical characterization (Figure 5.3a). The reference electrode (RE) and counter electrode (CE) are directly dipped into aCSF medium. The return electrode of the biointerface is connected to the working electrode (WE), and only 1 cm^2 of the biointerface is dipped into the aCSF solution through the measurements. Under 780 nm pulsed illumination, the biointerface produces a rapid capacitive peak, followed by a gradual decrease in the photocurrent profile (Figure 5.3b). The biointerface can generate 2.17 ± 0.2 $mA.cm^{-2}$ (mean ± SEM, n=10) and the rise time of the photocurrent is ~51 µs, indicating a strong capacitive behavior. Due to reversible faradaic reactions from the return electrode, photocurrent characteristics show a slow decrease after the fast-capacitive peak. This slow decrease significantly contributes to the total (ionic) charges generated in the electrolyte (i.e., aqueous biological medium of aCSF) when the light is turned on. The biointerface can produce a photovoltage peak of 237 ± 6 mV (mean ± SEM, n=10), and it can induce 10.97 ± 0.7 $\mu C.cm^{-2}$ charge (mean ± SEM, n=10) at 0.5 $mW.mm^{-2}$ (Figure 5.3b and c).

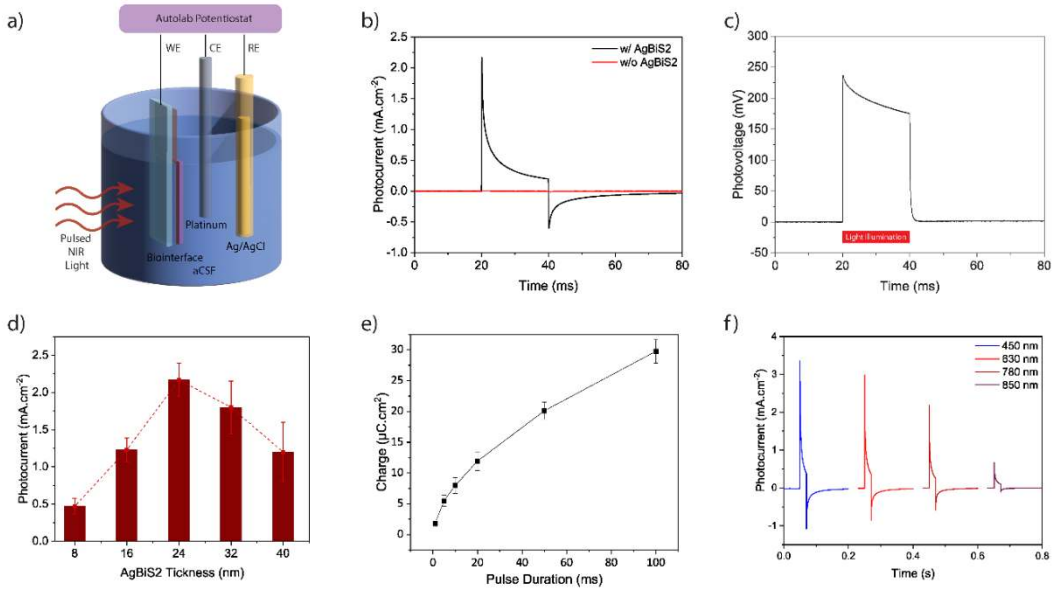

Figure 5.3 a) Photo-electrochemistry setup used for photovoltage and photocurrent characterization of the biointerface. b) Photocurrent response of the biointerface with ITO/ZnO/$AgBiS_2$/P3HT structure (Black line) and without $AgBiS_2$ (Red line) as control (Light illumination: 780 nm NIR, 20 ms, 0.5 $mW.mm^{-2}$). c) Photovoltage under 780 nm NIR light illumination (20 ms, 0.5 $mW.mm^{-2}$) (mean ± SEM, n=10). d) Photocurrent peak levels for different $AgBiS_2$ layer thickness under NIR light illumination (mean ± SEM, n=5). e) Charge and photocurrent with different illumination intensities using NIR light. f) Photocurrent under different illumination wavelengths.

For optimal photocurrent generation we investigated the thickness of the $AgBiS_2$ NC layer (Figure 5.3d). When the thickness of $AgBiS_2$ is below 16 nm, we observed a significant decrease in the photocurrent, which is attributed to the relatively low light absorption. When the thickness was higher than 32 nm, we observed drop of photocurrent. Hence, we used 24-nm-thick $AgBiS_2$ NCs for the fabrication of the photovoltaic bioelectronic devices. Other than $AgBiS_2$, each layer in the device is critical for optimal performance (Figure 5.4). For example, removing either ETL or HTL led to an almost 12-fold decrease in photocurrent (Figure 5.5) and addition of RuO_2 increases the charge for ~10 times compared to the biointerface in comparison with only ITO (Figure 5.6).

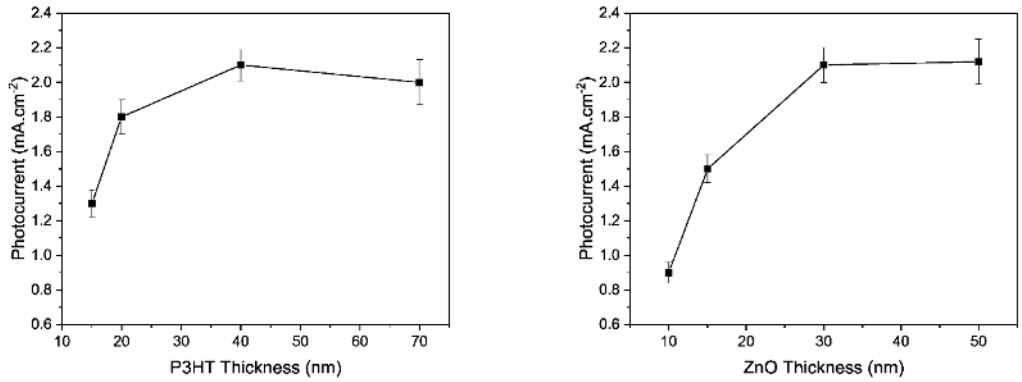

Figure 5.4 Photocurrent measurements for different P3HT a) and ZnO b) layer thickness under NIR light illumination (mean ± SEM, n=5).

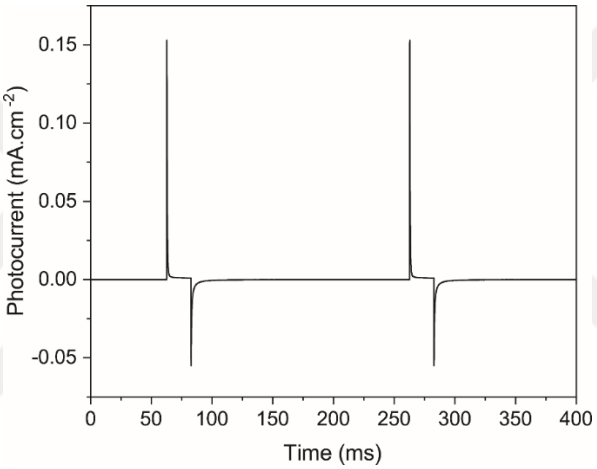

Figure 5.5 Photocurrent in the absence of ZnO electron transfer layer. The biointerface has the following structure: ITO/$AgBiS_2$/P3HT with ITO in the return electrode. Illumination condition: 20 ms, 780 nm, 0.5 $mW.mm^{-2}$.

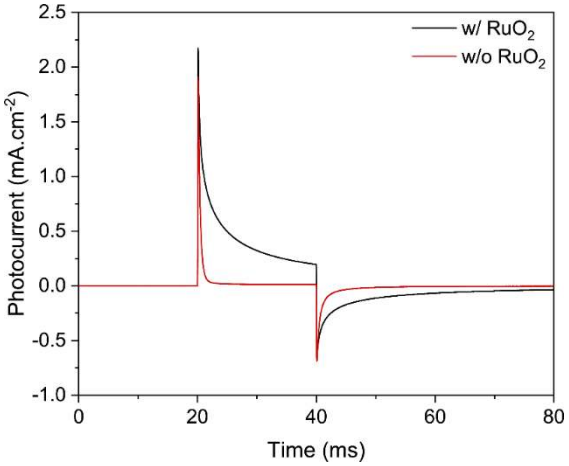

Figure 5.6 Photocurrent in the presence and absence of RuO_2 on the return electrode. Illumination condition: 20 ms, 780 nm, 0.5 $mW.mm^{-2}$.

Cyclic voltammetry (CV) and electrochemical impedance spectroscopy (EIS) are utilized in aCSF to show the successful RuO_2 coating in physiological settings (Figure 5.7). The symmetric and quasi-rectangular shapes of the cyclic voltammograms indicate the capacitive nature of the films with reversible redox reactions. Therefore, the ITO/ZnO/$AgBiS_2$/P3HT architecture with RuO_2 return electrode led to the high photoelectrical performance in terms of capacitive response and charge injection.

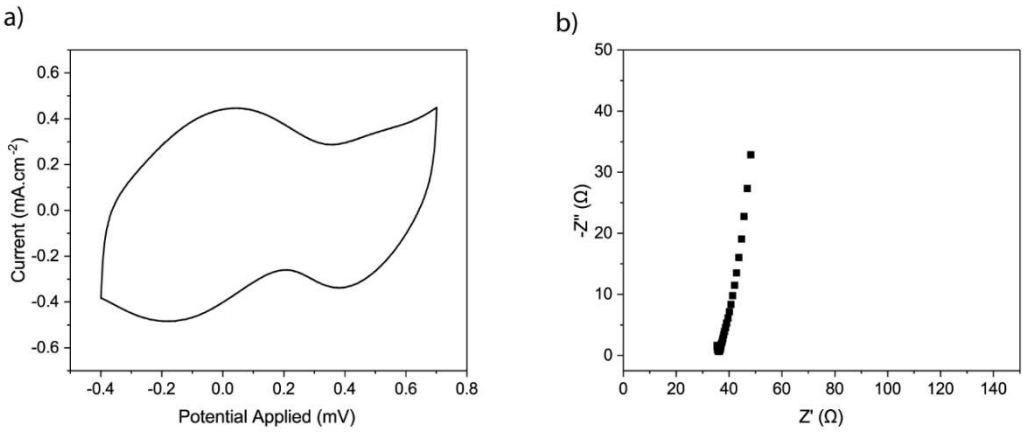

Figure 5.7 a) Cyclic voltammograms of RuO_2 coating from −0.4 to 0.7 V range. Scan rate is 50 mV s^{-1}. b) Electrochemical impedance measurement of RuO_2 coatings within the frequency range of 1–10 000 Hz.

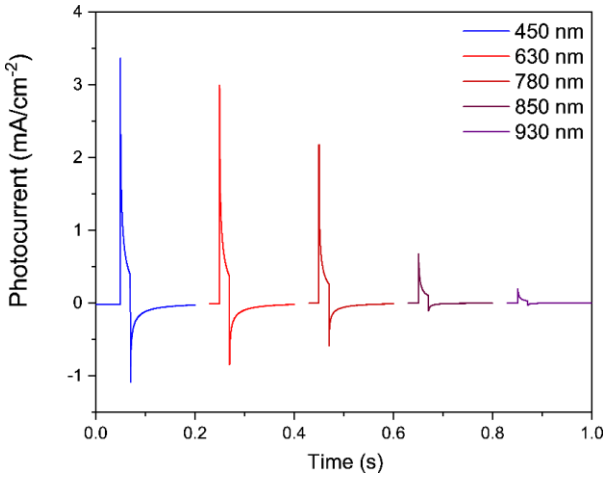

Figure 5.8 Photocurrent under different illumination wavelengths.

Charge generation level is another important criterion for effective stimulation of neurons and as the light intensity increases, the ionic charge injection increases (Figure 5.3e). The device can generate 5.9 µC.cm^{-2} even at low light levels of 0.1 mW.mm^{-2} at NIR, which is sufficiently high for neurostimulation in-vivo[89, 90]. Moreover, we

investigated photoresponse for different wavelengths (Figure 5.3f and Figure 5.8), and the biointerface generates a larger photocurrent of 450 nm because of the absorption of P3HT layer in blue and higher oscillator strength of $AgBiS_2$ NCs toward shorter wavelengths. The absorbance spectrum of the P3HT also shows that there is almost no absorption in NIR region (Figure 5.9), which proves that our device is operating under the NIR with the contribution only by the $AgBiS_2$ NC layer (Figure 5.9).

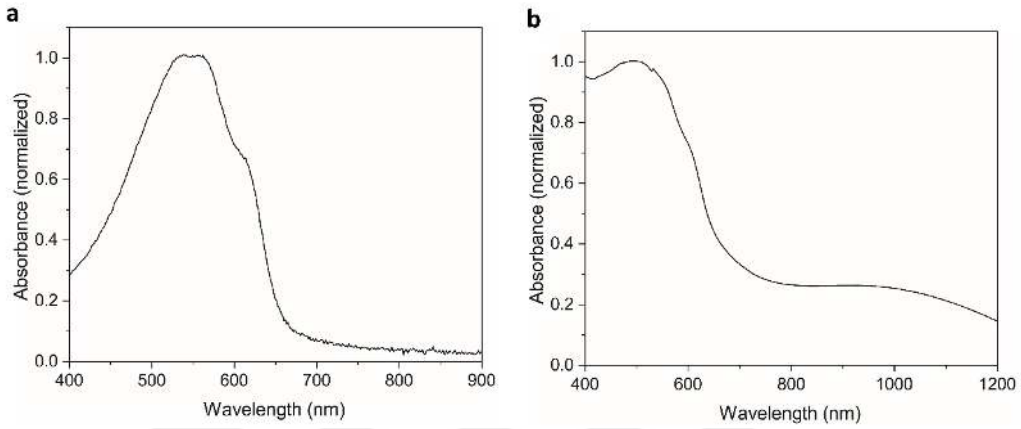

Figure 5.9 a) Absorbance of ITO/ZnO/P3HT. b) Absorbance of ITO/ZnO/$AgBiS_2$/P3HT showing that absorbance in NIR range is due to the contribution of $AgBiS_2$ NC layer.

We further investigated the photocurrent and charge generation of the biointerface in a standalone and wireless mode, similar to the working condition in cellular environments. A glass capillary as the counter electrode and a distant Ag/AgCl bath electrode as the reference were used to measure the photocurrent performance (Figure 5.10a). We measured the photocurrent with the illumination power of 2 $mW.mm^{-2}$ and obtained 13.7 ± 0.8 nA (mean ± SEM, n=10), with a high-level of charge injection confirming the electrochemical measurements (Figure 5.10b and c). To better understand the charge injection amount for different pulse configurations, we applied illuminations ranging from 1 to 1000 ms at 0.1 Hz (Figure 5.10d). We observed that as the pulse duration increases, the charge significantly rises as expected. Moreover, we observed less than 3% contribution by the faradaic contribution (e.g., 500 ms) indicating capacitive dominant charge transfer mechanism [27].

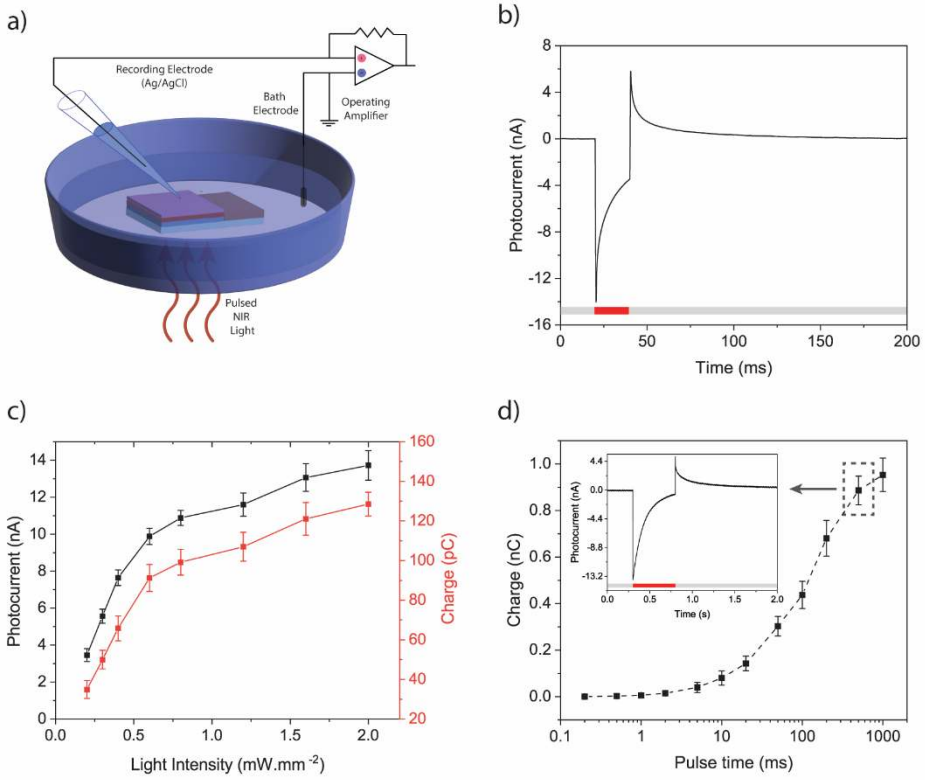

Figure 5.10 a) Photocurrent measurement via patch-pipette tip positioned close to the surface of the biointerface. b) Photocurrent of the biointerface under illumination. c) Photocurrent and charge of the biointerface depending on light intensity using 780 nm light illumination (mean ± SEM, n=10). d) Charge depending on pulse duration of the illumination (mean ± SEM, n=10).

5.3 Stability and biocompatibility

We investigated the photostability and biocompatibility of the devices without any encapsulation. For the long-term stability of the biointerface, we applied a passive accelerated ageing test. This involves placing the samples into a glass petri dish filled with H_2O_2 supplemented aCSF and exposing them to 87 °C oven under dark conditions for 680 h to simulate the ageing for 30 months[91]. The photocurrent was measured using chronoamperometry every 45-h simulating thirty months of ageing (Figure 5.11a). As a result, we observed a halftime of 12.5 years. We also tested the photostability of the device under long illumination cycles. Here, the charge and photovoltage remained around 80% compared to the initial values after 10^5 repetitive photoexcitation (Figure 5.11b)[27]. This behavior highlights the capacitive nature of the device, and high charge injection from the return electrode is due to reversible reactions. Before checking the

biocompatibility of the devices, we explored the effect of sterilization steps, which consisted of a five-minute of ethanol dip, UV treatment, PLL coating, and overnight cell medium in incubation (Figure 5.11c). The photocurrent results indicate that the performance of the device is mainly preserved after sterilization tests.

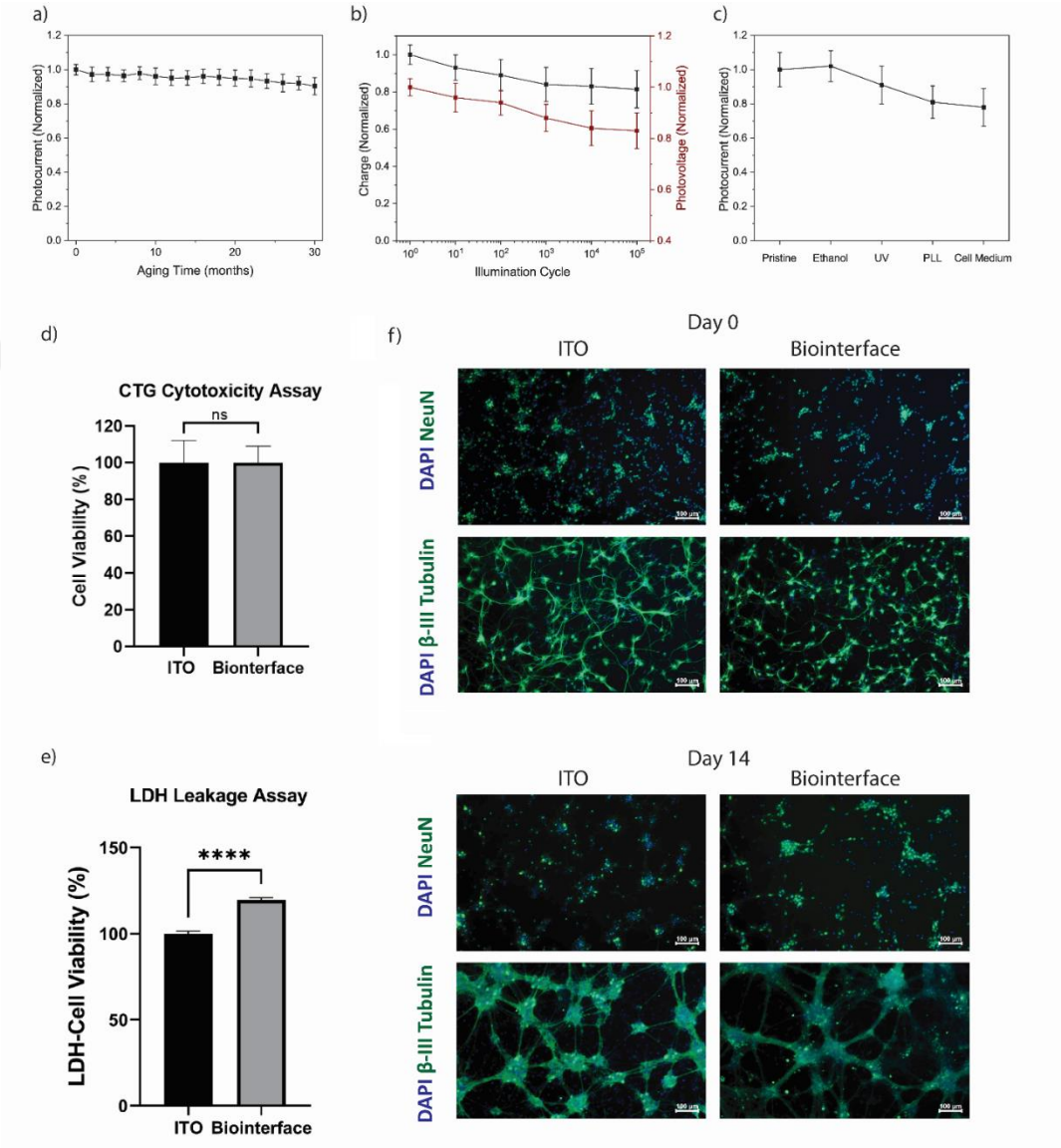

Figure 5.11 a) Photocurrent under passive accelerated ageing test. Biointerfaces were placed in physiological saline solution at 87 °C in dry oven under dark conditions for 680 h to age for 30 months. Chronopotentiometry measurements were repeated in each 45 h (mean ± SEM, n = 4). b) Photo-cyclic stability of the biointerface (mean ± SEM, n = 4) under the stimulus frequency of 100 Hz, pulse-width of 5 ms, optical power density of 2.5 $mW.mm^{-2}$. **c** Sterilization stability test, under ethanol dipping, UV sterilization, PLL coating, keeping in cell medium (3-day incubation). d) CTG cytotoxicity assay for quantifying cell viability of primary hippocampal neurons cultured on the ITO control

and the $AgBiS_2$ biointerface (mean ± SEM, n = 4). e) LDH leakage assay for measuring cell viability through cell membrane integrity of neurons on the substrates (mean ± SD for n = 5). An unpaired, two-tailed t-test was used for statistical analysis, and *$p < 0.05$ was evaluated as statistically significant. f) Immunofluorescence images at Day 0 and Day 14 of neurons cultured on the ITO and biointerface. Cells were co-stained with DAPI (blue) nuclear marker and Anti-NeuN (green) neuronal nuclear marker or co-stained with DAPI (blue) nuclear marker and Anti-beta III Tubulin (green) neuronal structure marker (scale bar: 100 μm).

Since in our previous studies we demonstrated that the use of P3HT on the biointerface had no adverse effect on cell survival[92, 93], at first we tested the effect of $AgBiS_2$ NCs on primary hippocampal cells by using devices without P3HT layer. Morphological features of neurons during 14-day culture period were maintained on ITO/ZnO/$AgBiS_2$ devices and showed no significant alteration in morphology with respect to the control group (Figure 5.12). Then, CTG cell viability and LDH leakage analysis were performed to examine the cytotoxicity of neurons growing on the ITO/ZnO/AgBiS2/P3HT with RuO_2. CTG test provides the cell viability depending on the amount of ATP in the cell populations, while LDH leakage test measures the release of lactate dehydrogenase (LDH) from cells in the culture environment. CTG measurement showed high viability of primary hippocampal neurons cultured on ITO control and biointerface (Figure 5.11d). We observed that the biointerfaces had no negative effect on the viability of primary hippocampal neurons via the LDH leakage test, which is consistent with CTG results. The amount of LDH leakage from cells cultured with the device was lower compared to the reference ITO control group indicating a high level of cell viability (Figure 5.11e).

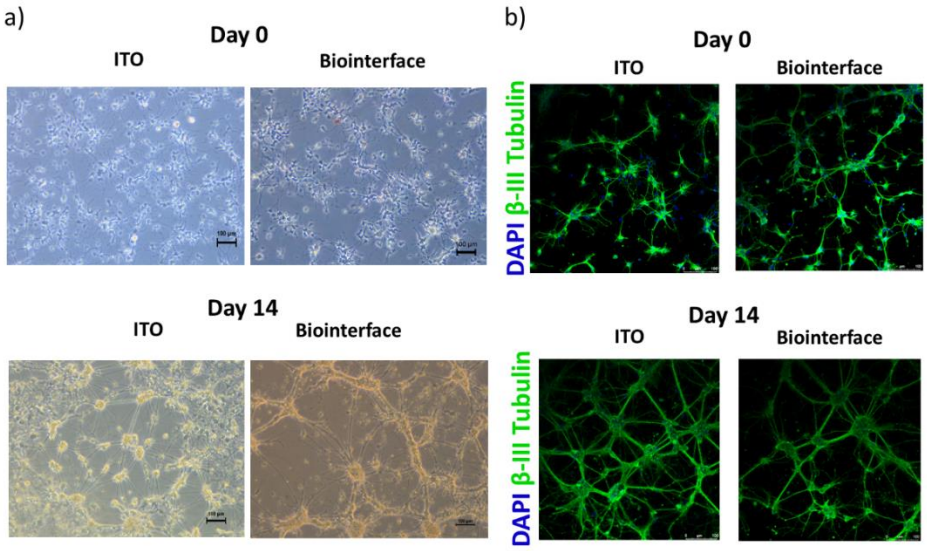

Figure 5.12 a) Bright field images of neurons on ITO control and biointerface during 2 weeks of the culture period (scale bar: 100 μm) and b) Immunofluorescence images at Day 0 and Day 14 of neurons cultured on the ITO and ITO/ZnO/$AgBiS_2$ devices. Cells were co-stained with DAPI (blue) nuclear marker and anti-β-III-Tubulin (green) neuronal structure marker (scale bar: 100 μm).

The short-term and long-term effect of the substrates on the cells (at day-0 and day-14, respectively) were monitored in terms of number of neurons, their characteristics and morphology. NeuN and beta-III-Tubulin staining was performed to examine the neuronal specific properties and functional changes. The cells remained healthy and viable during 14 days of culture period and conserved their specific characteristics with enlarged neuronal network both on ITO control and biointerface (Figure 5.11f). DAPI and NeuN positive cells were analyzed to show the number of neuron and total cells per unit area, and they remained similar throughout the 2-week culture period (Figure 5.13).

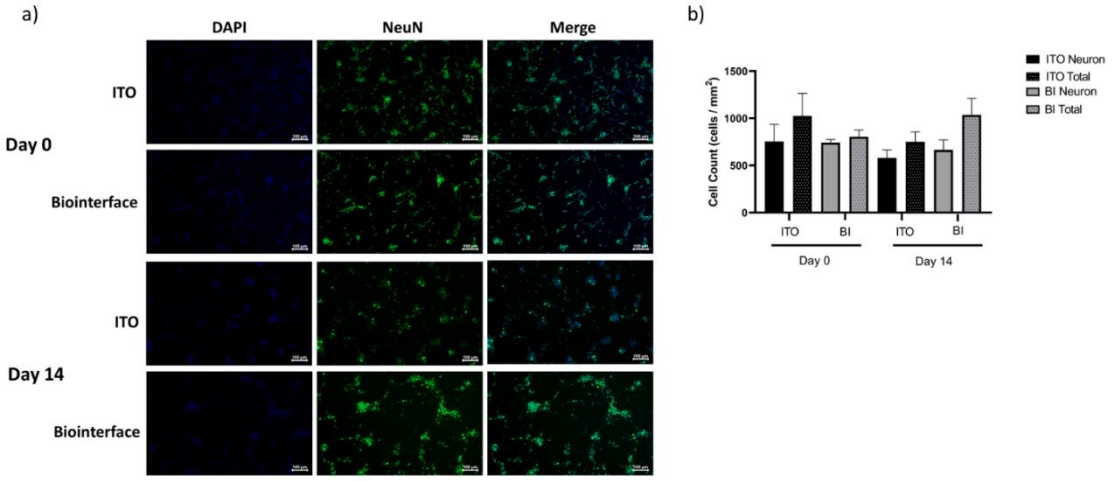

Figure 5.13 a) Immunofluorescence images at Day 0 and Day 14 of neurons cultured on the ITO and biointerface. Cells were co-stained with DAPI (blue) nuclear marker and Anti-NeuN (green) neuronal nuclear marker. b) Quantification of the number of NeuN positive cells and total number of cells per mm^2 for each culture period shown in immunofluorescence images (mean ± SD, n =4)

Neurite length analysis was carried out using anti-beta-III-Tubulin staining, during which neurites were traced from the perimeter of the soma to their endpoints. Cells and the growth of neurites exhibited similar distribution on both ITO and biointerface. In the first week of culture, the neurite extensions of the neurons on the ITO appear to significantly longer compared to the biointerface, however in the following days, it was observed that the connections between the axon extensions and cell populations were enhanced in the biointerface compared to ITO (Figure 5.14).

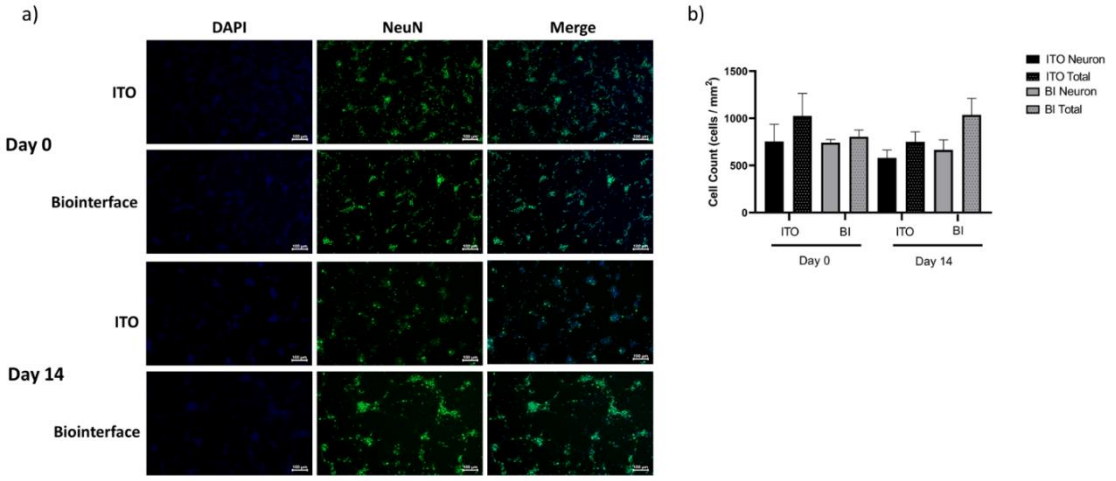

Figure 5.14 a) Immunofluorescence images at Day 0 and Day 14 of neurons cultured on the ITO and biointerface. Cells were co-stained with DAPI (blue) nuclear marker and Anti-beta III Tubulin (green) neuronal structure marker. b) Quantification of neurite length for each culture period were performed from immunofluorescence images (mean ± SD, n = 50 cells)

5.4 Single-cell electrophysiology recordings

We cultured primary hippocampal neurons on the biointerface to show light-induced neural stimulation. The primary neurons are well-accepted in vitro models to analyze action potential activities[94]. We utilized patch clamp electrophysiology experiments to record the electrical activity of the neurons on the biointerface under NIR illumination. First, the intracellular potential of the neurons is measured from the soma, where the reference Ag/AgCl bath electrode is placed inside the same extracellular solution distant from the biointerface (Figure 5.15a). The cells remained in the patch for an average of 5 ± 4 mins (mean ± SEM, n=10) without a significant change in the resting membrane potential. We recorded the transmembrane current under whole cell patch in voltage clamp mode (Figure 5.15b) and observed fast sodium current at -30 mV holding potential indicating that 40 mV of depolarization is required to excite the cell.

We record action potentials when the depolarization passes the threshold level (Figure 5.15c). The photogenerated holes are confined close to the surface of the biointerface and this positive charge induces hyperpolarization of the attached membrane while the recorded free membrane has depolarization[48]. Stimulation frequency is important for the success rate of neural activity, where a firing rate of 94.3 ± 1.9 % (mean

± SEM, n=10) is observed for 1 Hz illumination at an intensity level of 2.5 $mW.mm^{-2}$. For 25 Hz illumination it decreases to a 66.8 ± 3.1 % (mean ± SEM, n=10) (Figure 5.15d and e). While we change the intensity, the success rate of action potentials also varies. For example, the biointerface shows a success rate of 78.4 ± 4.4 % (mean ± SEM, n=10) at 1.5 $mW.mm^{-2}$ (Figure 5.15f), and when we decrease the intensity to 1 $mW.mm^{-2}$, the device is still able to trigger firing of neurons, which correspond to over an order of magnitude lower than the ocular safety limit at 780 nm (i.e., 18.75 $mW.mm^{-2}$).

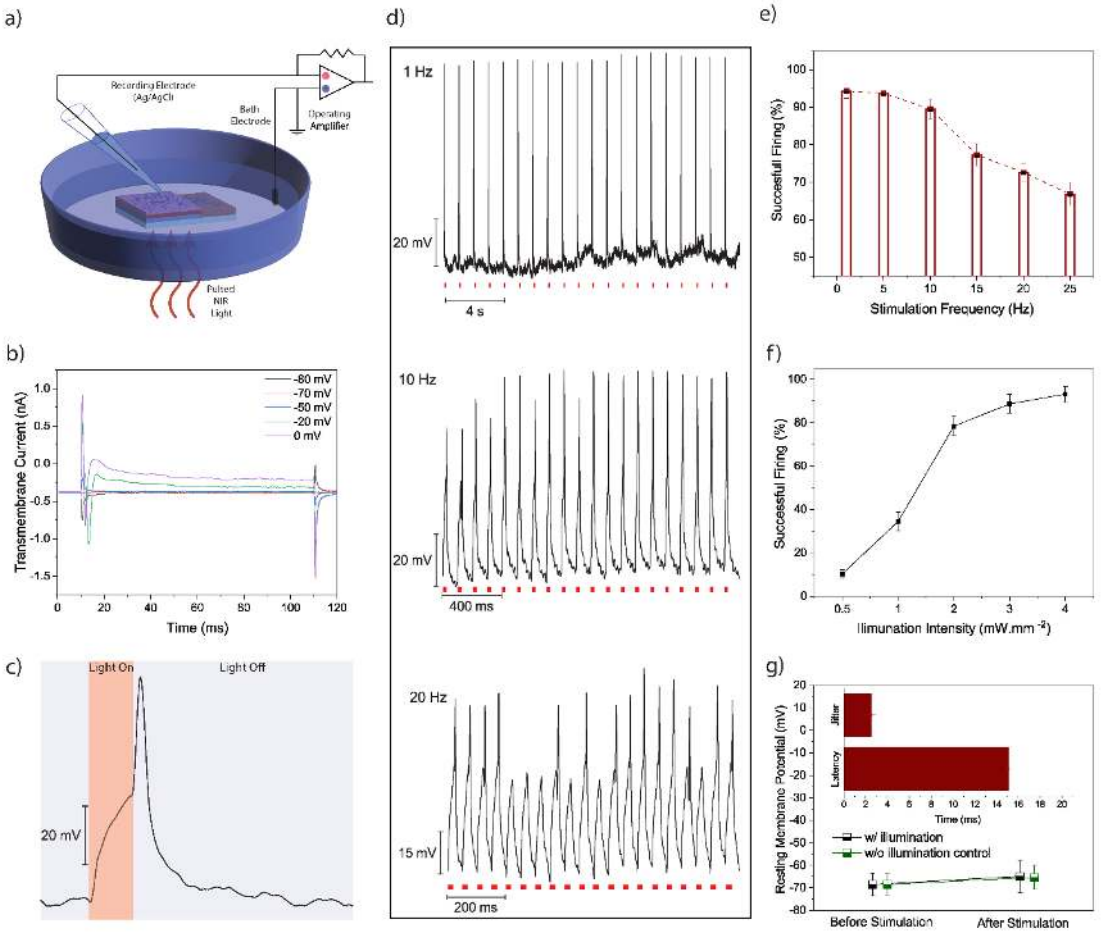

Figure 5.15 a) Single-cell patch-clamp electrophysiology recording of hippocampal neurons on the biointerface. b) Transmembrane current recording in whole-cell configuration by applying different holding potentials. **c** A typical action potential of neurons on the biointerface under 780 nm light illumination. d) Single cell electrophysiology recordings for different frequencies 1, 10, and 20 Hz (from top to down, respectively), with same pulse width of 20ms. e) Successful action potential firing versus stimulation frequency at 2.5 $mW.mm^{-2}$ (mean ± SEM, n=4 neurons). f) Action potential firing versus illumination intensity under NIR illumination at 5 Hz (mean ±

SEM, n=4 neurons). g) Resting membrane potential before and after stimulation. Inset: Spike latency and jitter of neuronal membrane induced by the biointerface (mean ± SEM, n=4 neurons).

To understand the temporal precision of neural stimulation, we analyzed the mean latency (time between stimulation onset and action potential peak) and jitter (standard deviation of latencies for all neurons) (Figure 5.15g inset). We found that the mean latency is 15.0 ± 3.6 ms (mean ± SEM) and jitter is 2.5 ± 0.4 ms (mean ± SEM, n=10). Considering recent methods like photothermal and photoacoustic stimulation, our latency value is much smaller and comparable with the ranges reported in optogenetics[95-97]. In addition, we applied one thousand pulses with a 5 Hz illumination frequency, and there was no significant change in resting membrane potential compared to control devices (Figure 5.15g). Since the maximum temperature increase using 2.5 $mW.mm^{-2}$ illumination can only change the temperature as 0.12°C[98], thermal increase does not have any significant contribution to the stimulation. We also observed no depolarization of neurons by the ITO control substrates under illumination (Figure 5.16). Thus, the device can operate within the safe limits under pulsed NIR light exposure (Figure 5.16)[49].

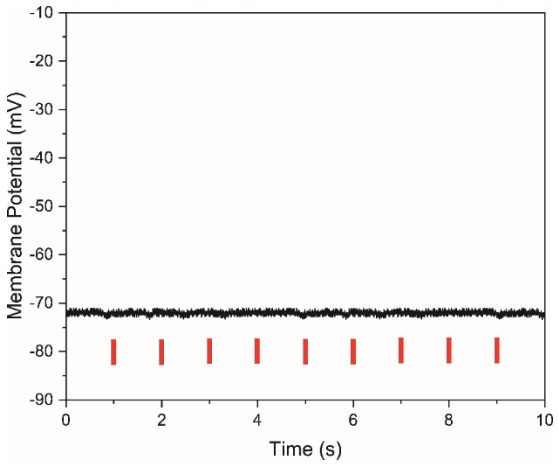

Figure 5.16 Single cell electrophysiology recordings measured from the cells cultured on control ITO devices. The frequency of illumination is 1 Hz.

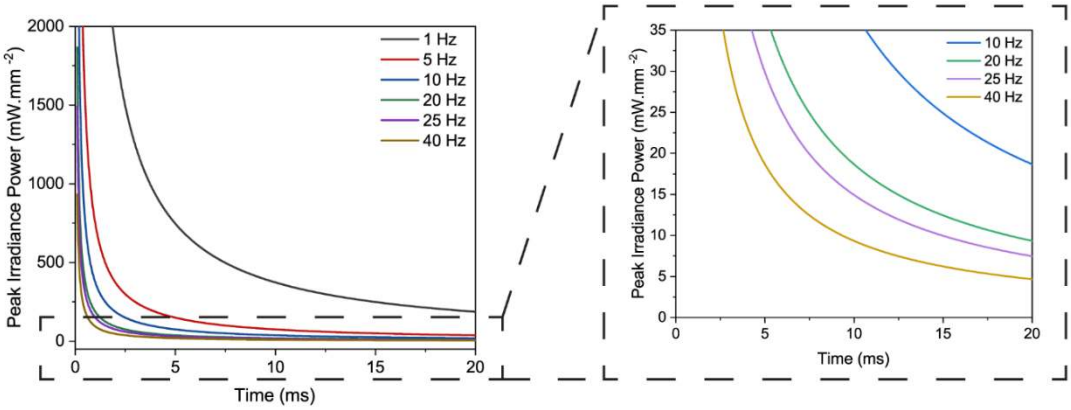

Figure 5.17 Calculated permissible light exposure based on ocular safety standards [8] for different pulse durations and frequencies at 780 nm.

NIR photostimulation of neurons is facilitated by $AgBiS_2$ nanocrystals that have the green heavy metal of bismuth[99] while toxic lead, mercury and cadmium heavy metal based NCs were used in previous reports[31]. Since $AgBiS_2$ NCs have absorption coefficient higher than other inorganic photovoltaic materials such as silicon, GaAs, InP, etc. in the NIR window ranging from 750 to 900 nm[87], such a strong absorption enabled an ultra-thin bioelectronic interface and the use of small quantities of the nanomaterials (~0.5 µg). Furthermore, the reduced thickness serves the additional purpose of minimizing the occupied volume of the implants that can potentially facilitate seamless integration.

The efficient photocurrent generation is critical to control the stimulation contrast of retina while operating below the ocular safety limit. In terms of quantum dots, this device, which has around 4-fold higher photocurrent than the previous PbS based optoelectronic biointerfaces[82], has the best light to electricity conversion reported device performance in NIR so far[31] (Table 5.1). Like quantum dots, organic semiconductors such as indigo dyes, polymers and silicon nanostructures are exciting materials for flexible photovoltaic neurostimulation devices, but they generally operate in the visible spectrum up to deep red[100-102]. Only one pioneering recent study using an bulk heterojunction photovoltaic device extended the spectral window toward NIR[103].

Table 5.1 Active layer thicknesses, photocurrent, and operational wavelengths from previous reports compared to this study.

References	Active layer Thickness	Photocurrent	Operational wavelength
This study	**24 nm**	**2.3 mA.cm^{-2}**	**780 nm**
[1]	30 nm	800 μA.cm^{-2}	630 nm
[2]	60 nm	2 mA.cm^{-2}	638 nm
[3]	25 nm	0.5 mA.cm^{-2}	780 nm
[4]	30 μm	9.2 mA.cm^{-2}	880 nm

Diseases that lead to the degeneration of the retina such as retinitis pigmentosa and AMD are the primary cause of the permanent loss of vision. NIR responsivity of the bioelectronic interfaces is critical to communicate with the retinal prosthetics implanted into patients[75]. For the patients with atrophic form of AMD, there are surviving photoreceptors that allow them to have peripheral vision. Since photoreceptors has around 5-orders-of-magnitude less sensitivity at the wavelength used in this study in comparison with the peak at 555 nm[104], NIR illumination can directly facilitate photostimulation of neurons without any interference with the remaining photoreceptors, and potentially enable perception of artificial vision[74]. The flexibility of such devices can open the possibility for large-area implementation into the retina and this leads to an extended field of view, which is advantageous for mobility and performing visually-driven search tasks of patients[105].

In conclusion, we demonstrated the first toxic-heavy-metal-free nanocrystal-based optoelectronic biointerface operating within the NIR spectral window. The extraordinary absorption strength of $AgBiS_2$ NCs allowed efficient photocurrent generation via a nanoscale NC layer (i.e., 24 nm). At the same time, the devices made of $AgBiS_2$ showed good biocompatibility and stability in cellular environment. Patch-clamp electrophysiology of primary hippocampal neurons enabled us to observe the modulation of membrane potential. These devices can induce successful photostimulation of primary hippocampal neurons at tens of hertz below the ocular safety limits. Hence, $AgBiS_2$ nanocrystals show high potential for future retinal prosthetics.

Chapter 6:
CONCLUSION

In this thesis, we explored the development innovative neuromorphic and photovoltaic neurostimulation devices, emphasizing their potential to be used in neuroprosthetic applications. Our research focused on creating compact, efficient, and biocompatible devices that can mimic the functionality of biological neurons while addressing the limitations of existing systems.

In the first part of the thesis, we showed a quantum dot-based artificial synapse (QDAS) biohybrid neuromorphic devices. By integrating memory, photodetection, and neurostimulation into a single photovoltaic biointerface, the QDAS can directly interface with neurons. This device facilitates short-term learning and modulates neuronal firing through Faradaic charge-transfer mechanisms, demonstrating its potential for future neuroprosthetics and soft robotics. This wireless device is particularly advantageous for implantation into tissues, offering a promising alternative to traditional wired systems that often require complex surgical operations.

Building on the principles of our first work, we worked on $AgBiS_2$ nanocrystals for NIR photostimulation. We showed the potential of this material for efficient and safe neurostimulation. With high absorption coefficient, $AgBiS_2$ integrated photovoltaic devices operates at NIR spectrum. We used solution processing, which helped us to produce ultra-thin bioelectronic interfaces, a crucial requirement for seamless integration into biological systems. These devices demonstrated excellent biocompatibility, stability, and effective modulation of neuronal activity, which makes them an excellent candidate for retinal prosthetics and other neurostimulation applications.

Our research also highlighted the potential of NIR-responsive bioelectronic interfaces for retinal prosthetics. Degeneration of the retina and eventual permanent loss of vision are caused by diseases such as retinitis pigmentosa and AMD. The flexibility of devices like $AgBiS_2$ nanocrystals allows for large-area implementation into the retina. These devices can potentially allow patients with AMD to gain artificial vision by photostimulating neurons while avoiding interference with the healthy photoreceptors by operating within the NIR spectral window.

In conclusion, the research presented in this thesis highlights the significant progress made in the fields of photovoltaic neurostimulation and neuromorphic photostimulation. The innovative use of nanomaterials, such as InP/ZnS core/shell quantum dots has paved the way for the development of unconventional and biomimetic neuroprosthetic devices and $AgBiS_2$ nanocrystals has been integrated into a photovoltaic bionterface for neurostimulation in NIR. These advancements offer new hope for improving the quality of life for individuals with neurological diseases and lay the groundwork for future research and development.

BIBLIOGRAPHY

1. Koch, C. and G. Laurent, *Complexity and the nervous system.* Science, 1999. **284**(5411): p. 96-98.
2. Patel, S.R. and C.M. Lieber, *Precision electronic medicine in the brain.* Nature biotechnology, 2019. **37**(9): p. 1007-1012.
3. Mallela, V.S., V. Ilankumaran, and N.S. Rao, *Trends in cardiac pacemaker batteries.* Indian pacing and electrophysiology journal, 2004. **4**(4): p. 201.
4. Zeng, F.-G., et al., *Cochlear implants: system design, integration, and evaluation.* IEEE reviews in biomedical engineering, 2008. **1**: p. 115-142.
5. Goyal, A., et al., *The development of an implantable deep brain stimulation device with simultaneous chronic electrophysiological recording and stimulation in humans.* Biosensors and Bioelectronics, 2021. **176**: p. 112888.
6. Lee, Y., et al., *A low-power stretchable neuromorphic nerve with proprioceptive feedback.* Nature Biomedical Engineering, 2023. **7**(4): p. 511-519.
7. Dai, S., et al., *Emerging iontronic neural devices for neuromorphic sensory computing.* Advanced Materials, 2023. **35**(39): p. 2300329.
8. Lee, Y. and T.-W. Lee, *Organic synapses for neuromorphic electronics: from brain-inspired computing to sensorimotor nervetronics.* Accounts of chemical research, 2019. **52**(4): p. 964-974.
9. Liao, F., et al., *Bioinspired in-sensor visual adaptation for accurate perception.* Nature Electronics, 2022. **5**(2): p. 84-91.
10. Balamur, R., et al., *A Retina-Inspired Optoelectronic Synapse Using Quantum Dots for Neuromorphic Photostimulation of Neurons.* Advanced Science, 2024. **11**(18): p. 2401753.
11. Park, H.L., et al., *Flexible neuromorphic electronics for computing, soft robotics, and neuroprosthetics.* Advanced Materials, 2020. **32**(15): p. 1903558.
12. Jung, Y.H., et al., *Bioinspired electronics for artificial sensory systems.* Advanced Materials, 2019. **31**(34): p. 1803637.
13. Lee, Y., et al., *A low-power stretchable neuromorphic nerve with proprioceptive feedback.* Nature Biomedical Engineering, 2022: p. 1-9.
14. Li, P., et al., *Bioinspired prosthetic interfaces.* Advanced Materials Technologies, 2020. **5**(3): p. 1900856.
15. Kim, K.N., et al., *Organic Synaptic Transistors for Bio-Hybrid Neuromorphic Electronics.* Advanced Electronic Materials, 2022. **8**(1): p. 2100935.
16. Kim, M.S., et al., *Bio-Inspired Artificial Vision and Neuromorphic Image Processing Devices.* Advanced Materials Technologies, 2022. **7**(2): p. 2100144.
17. Wan, C., et al., *An artificial sensory neuron with visual-haptic fusion.* Nature communications, 2020. **11**(1): p. 4602.
18. Lee, Y., et al., *Stretchable organic optoelectronic sensorimotor synapse.* Science advances, 2018. **4**(11): p. eaat7387.
19. Kim, Y., et al., *A bioinspired flexible organic artificial afferent nerve.* Science, 2018. **360**(6392): p. 998-1003.
20. Wang, Y., et al., *A rutile TiO2 electron transport layer for the enhancement of charge collection for efficient perovskite solar cells.* Angewandte Chemie International Edition, 2019. **58**(28): p. 9414-9418.

21. Choi, J., et al., *Well-defined nanostructured, single-crystalline TiO2 electron transport layer for efficient planar perovskite solar cells.* ACS nano, 2016. **10**(6): p. 6029-6036.
22. Kahmann, S. and M.A. Loi, *Trap states in lead chalcogenide colloidal quantum dots—origin, impact, and remedies.* Applied Physics Reviews, 2020. **7**(4).
23. Yu, S., et al., *Efficient photocatalytic hydrogen evolution with ligand engineered all-inorganic InP and InP/ZnS colloidal quantum dots.* Nature Communications, 2018. **9**(1): p. 4009.
24. Jalali, H.B., et al., *Past, present and future of indium phosphide quantum dots.* Nano Research, 2022. **15**(5): p. 4468-4489.
25. Cesca, F., et al., *The synapsins: key actors of synapse function and plasticity.* Progress in neurobiology, 2010. **91**(4): p. 313-348.
26. Srivastava, S.B., et al., *Band alignment engineers faradaic and capacitive photostimulation of neurons without surface modification.* Physical Review Applied, 2019. **11**(4): p. 044012.
27. Jiang, Y., et al., *Rational design of silicon structures for optically controlled multiscale biointerfaces.* Nature biomedical engineering, 2018. **2**(7): p. 508-521.
28. Han, M., et al., *Photovoltaic neurointerface based on aluminum antimonide nanocrystals.* Communications Materials, 2021. **2**(1): p. 19.
29. Karatum, O., et al., *Nanoengineering InP quantum dot-based photoactive biointerfaces for optical control of neurons.* Frontiers in neuroscience, 2021: p. 724.
30. Karatum, O., et al., *Quantum dot and electron acceptor nano-heterojunction for photo-induced capacitive charge-transfer.* Scientific Reports, 2021. **11**(1): p. 2460.
31. Han, M., O. Karatum, and S. Nizamoglu, *Optoelectronic Neural Interfaces Based on Quantum Dots.* ACS Applied Materials & Interfaces, 2022. **14**(18): p. 20468-20490.
32. Xu, S., S. Kumar, and T. Nann, *Rapid synthesis of high-quality InP nanocrystals.* Journal of the American Chemical Society, 2006. **128**(4): p. 1054-1055.
33. Tessier, M.D., et al., *Economic and Size-Tunable Synthesis of InP/ZnE (E= S, Se) Colloidal Quantum Dots.* Chemistry of Materials, 2015. **27**(13): p. 4893-4898.
34. Li, L. and P. Reiss, *One-pot synthesis of highly luminescent InP/ZnS nanocrystals without precursor injection.* Journal of the American Chemical Society, 2008. **130**(35): p. 11588-11589.
35. Suh, Y.H., et al., *Engineering core size of InP quantum dot with incipient ZnS for blue emission.* Advanced Optical Materials, 2022. **10**(7): p. 2102372.
36. Li, J., et al., *Enhancement of the photoresponse of monolayer MoS2 photodetectors induced by a nanoparticle grating.* ACS applied materials & interfaces, 2020. **12**(7): p. 8429-8436.
37. Shan, J., et al., *Enhanced photoresponse characteristics of transistors using CVD-grown MoS2/WS2 heterostructures.* Applied Surface Science, 2018. **443**: p. 31-38.
38. Lai, B.-C., J.-G. Wu, and S.-C. Luo, *Revisiting background signals and the electrochemical windows of Au, Pt, and GC electrodes in biological buffers.* ACS Applied Energy Materials, 2019. **2**(9): p. 6808-6816.

39. You, B. and Y. Sun, *Innovative strategies for electrocatalytic water splitting.* Accounts of chemical research, 2018. **51**(7): p. 1571-1580.
40. Santschi, L.A. and P.K. Stanton, *A paired-pulse facilitation analysis of long-term synaptic depression at excitatory synapses in rat hippocampal CA1 and CA3 regions.* Brain research, 2003. **962**(1-2): p. 78-91.
41. Luo, C., T. Kuner, and R. Kuner, *Synaptic plasticity in pathological pain.* Trends in neurosciences, 2014. **37**(6): p. 343-355.
42. Susumu, K., et al., *A new family of pyridine-appended multidentate polymers as hydrophilic surface ligands for preparing stable biocompatible quantum dots.* Chemistry of Materials, 2014. **26**(18): p. 5327-5344.
43. Rosenthal, S.J., et al., *Biocompatible quantum dots for biological applications.* Chemistry & biology, 2011. **18**(1): p. 10-24.
44. Garcia-Diosa, J.A., et al., *Influence of thickness, homogeneity, and morphology of TiO2-m nanoparticle coatings on cancer cell adhesion.* Surface and Coatings Technology, 2021. **427**: p. 127823.
45. Kommireddy, D., et al., *Layer-by-layer assembled nanoparticle thin films-a new surface modification approach for stem cell attachment.* Biomaterials, 2006. **27**(24): p. 4296-4303.
46. Kania, A., et al., *Effect of the Thickness of TiO2 Films on the Structure and Corrosion Behavior of Mg-Based Alloys.* Materials, 2020. **13**(5): p. 1065.
47. Byrne, J.H., *Chapter 16 - Postsynaptic Potentials and Synaptic Integration*, in *From Molecules to Networks (Third Edition)*, J.H. Byrne, R. Heidelberger, and M.N. Waxham, Editors. 2014, Academic Press: Boston. p. 489-507.
48. Schoen, I. and P. Fromherz, *The mechanism of extracellular stimulation of nerve cells on an electrolyte-oxide-semiconductor capacitor.* Biophysical journal, 2007. **92**(3): p. 1096-1111.
49. Delori, F.C., R.H. Webb, and D.H. Sliney, *Maximum permissible exposures for ocular safety (ANSI 2000), with emphasis on ophthalmic devices.* JOSA A, 2007. **24**(5): p. 1250-1265.
50. Besch, D., et al., *Extraocular surgery for implantation of an active subretinal visual prosthesis with external connections: feasibility and outcome in seven patients.* British Journal of Ophthalmology, 2008. **92**(10): p. 1361-1368.
51. Wang, B.-Y., et al., *Electronic photoreceptors enable prosthetic visual acuity matching the natural resolution in rats.* Nature Communications, 2022. **13**(1): p. 6627.
52. Vagni, P., et al., *POLYRETINA restores light responses in vivo in blind Göttingen minipigs.* Nature Communications, 2022. **13**(1): p. 3678.
53. Ayton, L.N., et al., *An update on retinal prostheses.* Clinical Neurophysiology, 2020. **131**(6): p. 1383-1398.
54. Parameswaran, R., et al., *Photoelectrochemical modulation of neuronal activity with free-standing coaxial silicon nanowires.* Nature Nanotechnology, 2018. **13**(3): p. 260-266.
55. Parameswaran, R., et al., *Optical stimulation of cardiac cells with a polymer-supported silicon nanowire matrix.* Proceedings of the National Academy of Sciences, 2019. **116**(2): p. 413-421.
56. Ashkan, K., et al., *Insights into the mechanisms of deep brain stimulation.* Nature Reviews Neurology, 2017. **13**(9): p. 548-554.

57. Ramirez-Zamora, A., et al., *Evolving applications, technological challenges and future opportunities in neuromodulation: proceedings of the fifth annual deep brain stimulation think tank.* Frontiers in Neuroscience, 2018: p. 734.
58. Nizamoglu, S., et al., *Bioabsorbable polymer optical waveguides for deep-tissue photomedicine.* Nature communications, 2016. **7**(1): p. 10374.
59. Liu, Z., et al., *Photoelectric cardiac pacing by flexible and degradable amorphous Si radial junction stimulators.* Advanced Healthcare Materials, 2020. **9**(1): p. 1901342.
60. Choi, M., et al., *Light-guiding hydrogels for cell-based sensing and optogenetic synthesis in vivo.* Nature photonics, 2013. **7**(12): p. 987-994.
61. Keene, S.T., et al., *A biohybrid synapse with neurotransmitter-mediated plasticity.* Nature Materials, 2020. **19**(9): p. 969-973.
62. Harikesh, P.C., et al., *Organic electrochemical neurons and synapses with ion mediated spiking.* Nature communications, 2022. **13**(1): p. 901.
63. Sarkar, T., et al., *An organic artificial spiking neuron for in situ neuromorphic sensing and biointerfacing.* Nature Electronics, 2022: p. 1-10.
64. Balamur, R., et al., *Capacitive and Efficient Near-Infrared Stimulation of Neurons via an Ultrathin AgBiS2 Nanocrystal Layer.* ACS Applied Materials & Interfaces, 2024.
65. Brocker, D.T. and W.M. Grill, *Principles of electrical stimulation of neural tissue.* Handbook of clinical neurology, 2013. **116**: p. 3-18.
66. Güemes Gonzalez, A., R. Etienne-Cummings, and P. Georgiou, *Closed-loop bioelectronic medicine for diabetes management.* Bioelectronic medicine, 2020. **6**: p. 1-7.
67. Won, S.M., et al., *Emerging modalities and implantable technologies for neuromodulation.* Cell, 2020. **181**(1): p. 115-135.
68. Karatum, O., et al., *Physical mechanisms of emerging neuromodulation modalities.* Journal of Neural Engineering, 2023.
69. Lee, J.S., et al., *Materials and device design for advanced phototherapy systems.* Advanced Drug Delivery Reviews, 2022. **186**: p. 114339.
70. Karatum, O., et al., *Optical neuromodulation at all scales: from nanomaterials to wireless optoelectronics and integrated systems.* Chemical Society Reviews, 2023.
71. Silverå Ejneby, M., et al., *Chronic electrical stimulation of peripheral nerves via deep-red light transduced by an implanted organic photocapacitor.* Nature Biomedical Engineering, 2022. **6**(6): p. 741-753.
72. Han, M., et al., *Tissue-like Optoelectronic Neural Interface Enabled by PEDOT: PSS Hydrogel for Cardiac and Neural Stimulation.* Advanced Healthcare Materials, 2021: p. 2102160.
73. Jo, Y.J., et al., *Biocompatible and biodegradable organic transistors using a solid-state electrolyte incorporated with choline-based ionic liquid and polysaccharide.* Advanced Functional Materials, 2020. **30**(29): p. 1909707.
74. Palanker, D., et al., *Simultaneous perception of prosthetic and natural vision in AMD patients.* Nature communications, 2022. **13**(1): p. 513.
75. Huang, T.W., et al., *Vertical-junction photodiodes for smaller pixels in retinal prostheses.* Journal of neural engineering, 2021. **18**(3): p. 036015.
76. Prévot, P.-H., et al., *Behavioural responses to a photovoltaic subretinal prosthesis implanted in non-human primates.* Nature biomedical engineering, 2020. **4**(2): p. 172-180.

77. Bareket, L., et al., *Semiconductor nanorod–carbon nanotube biomimetic films for wire-free photostimulation of blind retinas.* Nano letters, 2014. **14**(11): p. 6685-6692.
78. Lugo, K., et al., *Remote switching of cellular activity and cell signaling using light in conjunction with quantum dots.* Biomedical optics express, 2012. **3**(3): p. 447-454.
79. Karatum, O., et al., *Nanoengineering InP quantum dot-based photoactive biointerfaces for optical control of neurons.* Frontiers in Neuroscience, 2021. **15**: p. 652608.
80. Pappas, T.C., et al., *Nanoscale engineering of a cellular interface with semiconductor nanoparticle films for photoelectric stimulation of neurons.* Nano letters, 2007. **7**(2): p. 513-519.
81. Merrill, D.R., M. Bikson, and J.G. Jefferys, *Electrical stimulation of excitable tissue: design of efficacious and safe protocols.* Journal of neuroscience methods, 2005. **141**(2): p. 171-198.
82. Karatum, O., et al., *Electrical Stimulation of Neurons with Quantum Dots via Near-Infrared Light.* ACS Nano, 2022. **16**(5): p. 8233-8243.
83. Truong, L., et al., *Differential stability of lead sulfide nanoparticles influences biological responses in embryonic zebrafish.* Archives of toxicology, 2011. **85**: p. 787-798.
84. Hu, R., et al., *PEGylated phospholipid micelle-encapsulated near-infrared PbS quantum dots for in vitro and in vivo bioimaging.* Theranostics, 2012. **2**(7): p. 723.
85. Wang, Y., et al., *Cation disorder engineering yields AgBiS2 nanocrystals with enhanced optical absorption for efficient ultrathin solar cells.* Nature Photonics, 2022: p. 1-7.
86. Bernechea, M., et al., *Solution-processed solar cells based on environmentally friendly AgBiS2 nanocrystals.* Nature Photonics, 2016. **10**(8): p. 521-525.
87. Wang, Y., et al., *Cation disorder engineering yields AgBiS2 nanocrystals with enhanced optical absorption for efficient ultrathin solar cells.* Nature Photonics, 2022. **16**(3): p. 235-241.
88. Karatum, O., et al., *RuO2 Supercapacitor Enabled Flexible, Safe, and Efficient Optoelectronic Neural Interface.* Advanced Functional Materials, 2022: p. 2109365.
89. Cogan, S.F., *Neural stimulation and recording electrodes.* Annu. Rev. Biomed. Eng., 2008. **10**: p. 275-309.
90. Yu, N., et al., *Near-infrared-light activatable nanoparticles for deep-tissue-penetrating wireless optogenetics.* Advanced healthcare materials, 2019. **8**(6): p. 1801132.
91. Lu, S., et al., *Accelerated discovery of stable lead-free hybrid organic-inorganic perovskites via machine learning.* Nature communications, 2018. **9**(1): p. 3405.
92. Kaya, L., et al., *MnO2 Nanoflower Integrated Optoelectronic Biointerfaces for Photostimulation of Neurons.* Advanced Science, 2023. **10**(25): p. 2301854.
93. Karatum, O., et al., *RuO2 supercapacitor enables flexible, safe, and efficient optoelectronic neural interface.* Advanced Functional Materials, 2022. **32**(31): p. 2109365.
94. Carvalho-de-Souza, J.L., et al., *Photosensitivity of neurons enabled by cell-targeted gold nanoparticles.* Neuron, 2015. **86**(1): p. 207-217.

95. Jiang, Y., et al., *Neural stimulation in vitro and in vivo by photoacoustic nanotransducers.* Matter, 2021. **4**(2): p. 654-674.
96. Wu, X., et al., *Tether-free photothermal deep-brain stimulation in freely behaving mice via wide-field illumination in the near-infrared-II window.* Nature Biomedical Engineering, 2022. **6**(6): p. 754-770.
97. Boyden, E.S., et al., *Millisecond-timescale, genetically targeted optical control of neural activity.* Nature neuroscience, 2005. **8**(9): p. 1263-1268.
98. Martino, N., et al., *Photothermal cellular stimulation in functional bio-polymer interfaces.* Scientific reports, 2015. **5**(1): p. 8911.
99. Wang, R., H. Li, and H. Sun, *Bismuth: environmental pollution and health effects.* Encyclopedia of environmental health, 2019: p. 415.
100. Jakešová, M., et al., *Optoelectronic control of single cells using organic photocapacitors.* Science advances, 2019. **5**(4): p. eaav5265.
101. DiFrancesco, M.L., et al., *A hybrid P3HT-graphene interface for efficient photostimulation of neurons.* Carbon, 2020. **162**: p. 308-317.
102. Chenais, N.A.L., M.J.I. Airaghi Leccardi, and D. Ghezzi, *Photovoltaic retinal prosthesis restores high-resolution responses to single-pixel stimulation in blind retinas.* Communications Materials, 2021. **2**(1): p. 28.
103. Airaghi Leccardi, M.J.I., et al., *Photovoltaic organic interface for neuronal stimulation in the near-infrared.* Communications Materials, 2020. **1**(1): p. 21.
104. Schubert, E.F., *Light-Emitting Diodes (2018)*. 2018: E. Fred Schubert.
105. Ghezzi, D., *The role of the visual field size in artificial vision.* Journal of Neural Engineering, 2023. **20**(2): p. 023001.